Available online at www.sciencedirect.com

jmr&t Journal of Materials Research and Technology

journal homepage: www.elsevier.com/locate/jmrt

Original Article

Analysis of the influence of L-PBF porosity on the mechanical behavior of AlSi10Mg by XRCT-based FEM

Alejandro Pascual [a,b,*], *Naiara Ortega* [b], *Soraya Plaza* [b], *Luis Norberto López de Lacalle* [b], *Eneko Ukar* [b]

[a] *Aeronautics Advanced Manufacturing Center, CFAA (UPV/EHU), Bizkaia Technology Park, Building 202, Zamudio 48170, Spain*

[b] *Faculty of Engineering of Bilbao, UPV/EHU, Plaza Torres Quevedo 1, Bilbao 48013, Spain*

ARTICLE INFO

Article history:
Received 5 October 2022
Accepted 28 November 2022
Available online 5 December 2022

Keywords:
X-ray computerized tomography
Porosity
Laser-powder bed fusion
AlSi10Mg
Mechanical behavior
Finite element modeling

ABSTRACT

This work aims to present an XRCT-based FEM methodology to assess the influence of porosity defects on the mechanical behavior and failure of L-PBF AlSi10Mg components. Hence, the influence of defects on performance is estimated by means of XRCT scanning and analysis of porosity features, followed by mechanical FEM modelling of digitalized components. For this purpose, some test specimens with induced artificial porosity were manufactured by L-PBF, according to ASTM E8/E8M. Once this is done, inspection and defect characterization were carried out by means of XRCT. Porosity features such as void size, shape and location, apart from porosity percentage, were analyzed. Then, tensile tests were carried out, followed by further inspections by XRCT in order to research the relationship between the fracture level and the porosity of the as-built sample. Afterwards, virtual tensile tests of XRCT-ed specimens were modeled by FEM technique. Results obtained by the FEM model were well-correlated with the tensile experimental results to predict both ultimate tensile strength and elongation at fracture of each specimen, showing errors below 5.2%. However, the results of the final fracture level predicted by FEM analysis reveal that possibly underestimated and/or non-detected defects on the AlSi10Mg specimens seem to influence the accuracy of the fracture level prediction in some samples. Thus, XRCT arises as an ideal technology for the assessment of L-PBF-ed components.

1. Introduction

Currently, decreasing greenhouse gas emissions has become the main challenge of the industrial sector, especially in automotive and aeronautical sectors [1]. Efforts have been devoted to promote components weight reduction, without disregarding safety [2,3]. This encourages the efficiency of engines, reducing energy consumption per unit distance. On the other hand, medical sector demands flexibility and tailored

* Corresponding author.
E-mail address: alejandro.pascual@ehu.eus (A. Pascual).

https://doi.org/10.1016/j.jmrt.2022.11.172

solutions for each patient [4–6]. In both cases, the advances in materials, design and manufacturing systems allow producing suitable components that satisfy the requirements with impressive waste reduction. Therefore, this approach is closely aligned with the concept of circular economy.

Against this background, lightweight material solutions are being developed. Aluminum alloys and Advanced High Strength Steels (AHSS) have been introduced in the automotive industry for this purpose [7]. Furthermore, composites are increasingly being used in the aeronautical sector. Regarding innovative design techniques, methodologies such as generative design [8], biomimetic design [9] or topology optimization [10–12] have arisen. In this context, additive manufacturing (AM) is emerging as the preferred technology due to its ability to define complex shapes with internal geometries, allowing the use of design methods stated above [13,14]. In contrast with subtractive manufacturing technologies, AM is based on adding only the necessary material enabling the reduction of scrap.

There are different AM techniques available. However, Laser Powder Bed Fusion (L-PBF), also called Selective Laser Melting (SLM), has received considerable attention in recent years. This interest is mainly due to its potential for manufacturing extreme complex shapes including thin walls and hollow structures. Honeycombs, lattice, scaffolds or provoked porous structures [15,16] are some examples. Thus, this technique is well-founded for manufacture critical components like combustion chambers, turbine blades [2] or customized medical implants (really interesting due to osseointegration [6]).

Nonetheless, AM processes are also subjected to the unexpected appearance of defects during the manufacturing process [17–20]. Although L-PBF aims to produce fully dense components, the avoidance of porosity defects is sometimes a difficult task [21–24]. According to Ref. [18], AM porosity defects are classified into two different groups: gas induced porosity and Lack-of-fusion (LoF) porosity. The first one is related to nearly spherical voids, which usually come from trapped gas between powder particles or directly arise from gas present inside powder particles. On the other hand, LoF pores show irregular shapes and their origin is usually associated to under-melting occurrences.

The presence of porosity defects induced during the manufacturing process of industrial components compromises their performance [25,26]. These defects produce geometrical discontinuities, which yield stress concentrations that promote the failure of the component driven by void growth and coalescence. Therefore, porosity defects have an impressive effect on the components structural integrity, especially regarding mechanical properties such as stiffness, strength, fatigue strength and toughness [27–30].

Focusing on porosity defects analysis, the porosity percentage, pore size and distribution are some of the most common indicators to assess the mechanical behavior of the components [28]. However, there are some aspects such as pore shape, location and orientation, which have an even greater influence on the stress concentrations produced by pores [31–35]. Considering this, under the same circumstances, LoF porosity is more detrimental than gas induced porosity since irregular void shapes increase the stress concentrations [36]. Moreover, special attention is to be paid on the loading direction, which defines the effect of pores on the stress concentrations according to the porosity aspects defined, especially according to the void shape.

Hence, the accurate detection, characterization and measurement of these defects enable to carry out truthful predictions of the mechanical behavior of the component.

In this framework, X-ray computerized tomography (XRCT) is increasingly being used as Non-Destructive Testing method (NDT), due to its ability to inspect internal and external features [25,37,38]. This advantage allows not only the qualitative analysis of defects, but also the quantitative one by dimensioning and locating each defect in the virtual reconstruction of the scanned part. Moreover, this technique provides the digital 3D volume of the scanned part, which could be used for several engineering applications such as dimensional metrology and quality control, reverse engineering or FEM analysis [39–42], amongst others.

This work aims to develop a methodology to predict the mechanical behavior of components of AlSi10Mg manufactured by L-PBF. To do it, tensile samples with induced porosity were inspected and digitalized by XRCT. Thus, the proposed XRCT-based FEM allows estimating the influence of different porosity aspects such as size, shape and spacing of each void on the mechanical behavior of the component.

2. Methodology

2.1. Description of the specimens design

In order to investigate the effect of porosity on the mechanical behavior of L-PBF manufactured parts, artificial voids were provoked. Next, description of each type of voids is provided.

8 sample geometries were manufactured. To analyze the repeatability, three samples of each type of artificial porosity were manufactured. One of them was defined without voids, while the other seven ones were designed with different homogeneous porosity distributions. The number of voids and location (center) of each one remain constant. Only the voids size and shape were modified in each test specimen. The schematic representation of void distributions and shape types are presented in Fig. 1. The details of the dimensions of the specimens and of each type artificial void are provided in Table 1.

AlSi10Mg was the material selected for the study. AlSi10Mg is a casting alloy which is also the most used L-PBF Aluminum alloy [43]. It is a hardenable alloy which exhibits high strengths, optimal resistance in corrosive atmospheres, high thermal conductivity and good weldability. Because of its properties, it is frequently used for thin-walled lightweight components and parts with complex geometries, especially for applications in aerospace engineering and the automotive industry [44].

The chemical composition of AlSi10Mg is presented in Table 2.

2.2. Manufacturing process

Regarding the manufacturing process, L-PBF technology was selected. A Renishaw AM500 (Renishaw, Wotton-under-Edge, UK) equipped with a 500 W Ytterbium fibre laser beam was used. Normal powder size distributions of 20–63 μm were

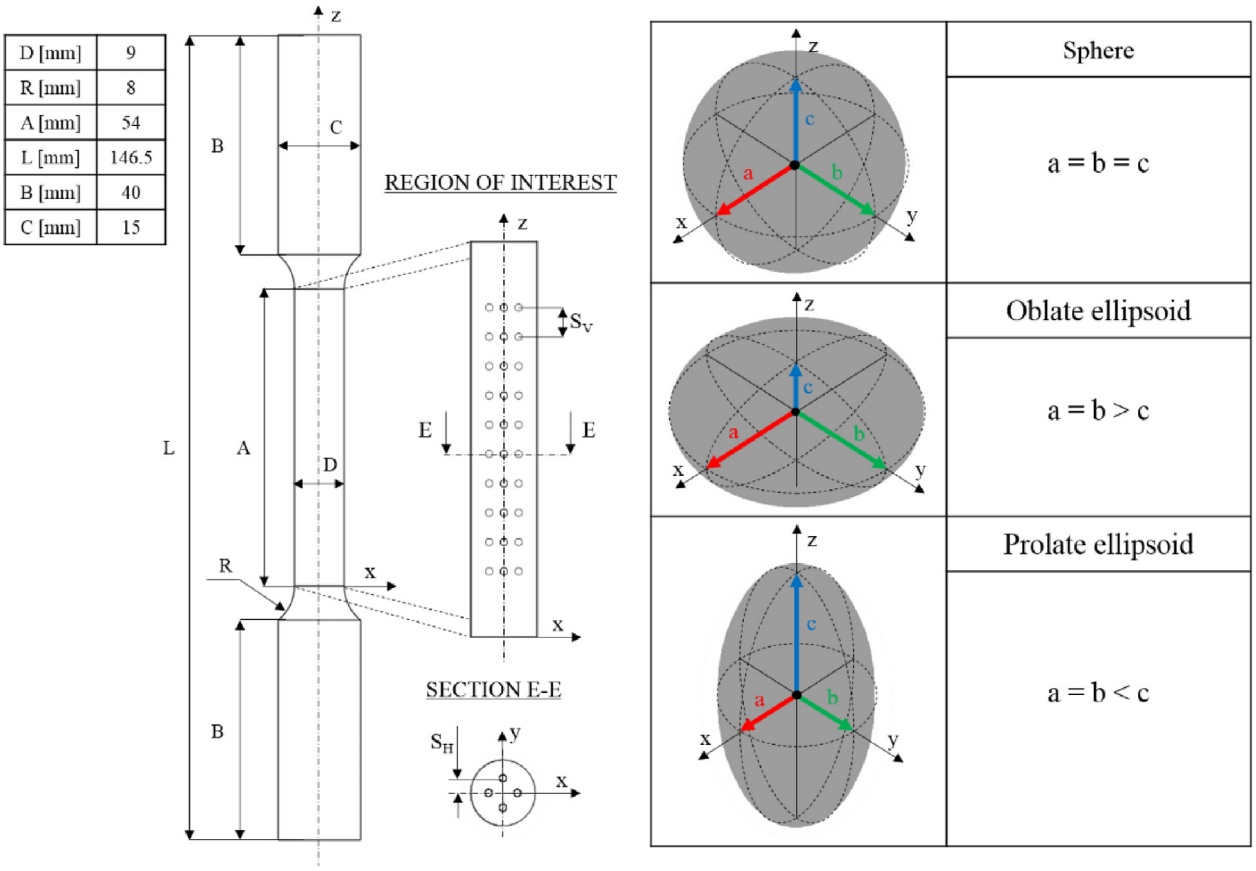

Fig. 1 – Test specimen dimensions according to ASTM E8/E8M and schematic representation of void distribution and shape types.

Table 1 – Test specimens void size, shape and distribution.

Code	Void shape	Void size [mm]			S_V distance [mm]	S_H distance [mm]	Number of voids	Porosity percentage[b] [%]
		a	b	c				
O1	–	–	–	–	–	–	–	–
A2	Sphere	0.5	a	a	4	2	40	0.610
A3	Oblate ellipsoid	0.5t[a]	a	a/2	4	2	40	0.610
A4	Prolate ellipsoid	0.5/t[a]	a	2a	4	2	40	0.610
B2	Sphere	0.4	a	a	4	2	40	0.312
B3	Oblate ellipsoid	0.4t[a]	a	a/2	4	2	40	0.312
C2	Sphere	0.15	a	a	4	2	40	0.016
C3	Oblate ellipsoid	0.15t[a]	a	a/2	4	2	40	0.016

[a] $t = 2^{\frac{1}{3}}$.
[b] Calculated in the region of interest.

Table 2 – Chemical composition of AlSi10Mg (wt. in %).

AlSi10Mg							
Al	Si	Fe	Cu	Mn	Mg	Zn	Ti
Balance	9.00–11.00	0.55	0.05	0.45	0.20–0.45	0.10	0.15
Ni	Pb	Sn	Other				
0.05	0.05	0.05	0.15				

employed. The layer thickness was set at 60 μm and the laser paths were modified 67° between layers. A spot size of 80 μm was utilized. For inner areas of each layer, filling stripes strategy with 27 μm of hatching distance was defined. Instead, boundaries and surrounding areas were established by contour path planning. 200 W of laser power was defined for the manufacturing process, according to the material requirements. Apart from that, the specimen main axis was set vertically, as well as the system building direction. Finally, test

specimens were sandblasted by the Nordblast SD9 blasting machine (Norblast, Bologna, Italy), using white corundum WSK 80 as blasting material.

2.3. XRCT inspection procedure

The inspection of the as-built specimens was performed by means of XRCT. It is based on the reconstruction of a 3D voxel volume from the projection images acquired during the scanning of the object. It is worth mentioning that the transmission of X-rays through the material is governed by the attenuation coefficient, which depends on the thickness, density and atomic number of the material. Thus, the X-ray scanning conditions should be set to be able to penetrate the scanned object with sufficient contrast. It enables to achieve quality projections for the further XRCT reconstruction. The XRCT scanning process is displayed in Fig. 2.

For the scanning purpose, a General Electric X-Ray machine model X-Cube Compact (Baker Hughes, Houston, TX, USA) was utilized. The scanning conditions are summarized in Table 3. Finally, the software VGStudio MAX 3.4 (Volume Graphics, Heidelberg, Germany) was used for XRCT data processing. VGEasyPore algorithm was used for porosity analysis.

Table 3 – Scanning conditions of XRCT inspection.

Specimens	AlSi10Mg
Focal spot size [mm]	0.4
Hardware filters	1 mm Cu and 0.5 mm Sn
Voltage [kV]	150
Current [mA]	4.0
Exposure time [ms]	100
Projections	720
Magnification	2.231

2.4. XRCT-based FEM

A FEM model from the results of the scanned part by XRCT was, then, programmed. The main advantage of the FEM model containing the digitalization of the real part is that it enables to get more accurate, reliable and representative models than conventional FEM models developed from computer-aided design (CAD) usually containing simpler geometries [45–48]. Thus, this approach improve the predictions of the component behavior.

To address this issue, the following steps of XRCT-based FEM definition are detailed.

2.4.1. XRCT-based meshing

There are different methods for image-based meshing in order to obtain unstructured or structured meshes. Unstructured meshes are comprised of triangular (2D) or tetrahedral (3D) elements, which present an irregular pattern. This approach is commonly accomplished using Delaunay-based, advancing-front base or octree-based methods. In contrast, structured meshes are composed of quadrilateral (2D) or hexahedral (3D) elements that follow a uniform pattern. In this case, the best known methods are the pixel-based (2D) and voxel-based (3D) meshing methods. Although the complex shapes accuracy is limited by these methods, they are preferred due to their computational efficiency [49,50].

Once the XRCT data is segmented, two different results are provided: triangular mesh surfaces and classified voxel volume. From the first option, unstructured meshes with tetrahedral elements are typically generated (see Fig. 3a)). On the other hand, structured meshes with hexahedral elements are used from the second option, which provides a brick model (see Fig. 3b)). In both cases, the accuracy of the results depends on the mesh refinement.

Alternatively, a CAD-based approach is also considered, as it takes advantage of meshing algorithms developed for this purpose. This method focuses on meshing a CAD model generated from XRCT data by means of reverse engineering solutions utilized for CAD model building (see Fig. 3c)).

The proposed approach was focused on reproduce the porosity aspects studied by XRCT analysis in the virtual reconstruction of the specimen. To do this, reverse engineering strategy was utilized by using CAD modelling techniques, such as sewing, stitching and boolean operations. Finally, due to the

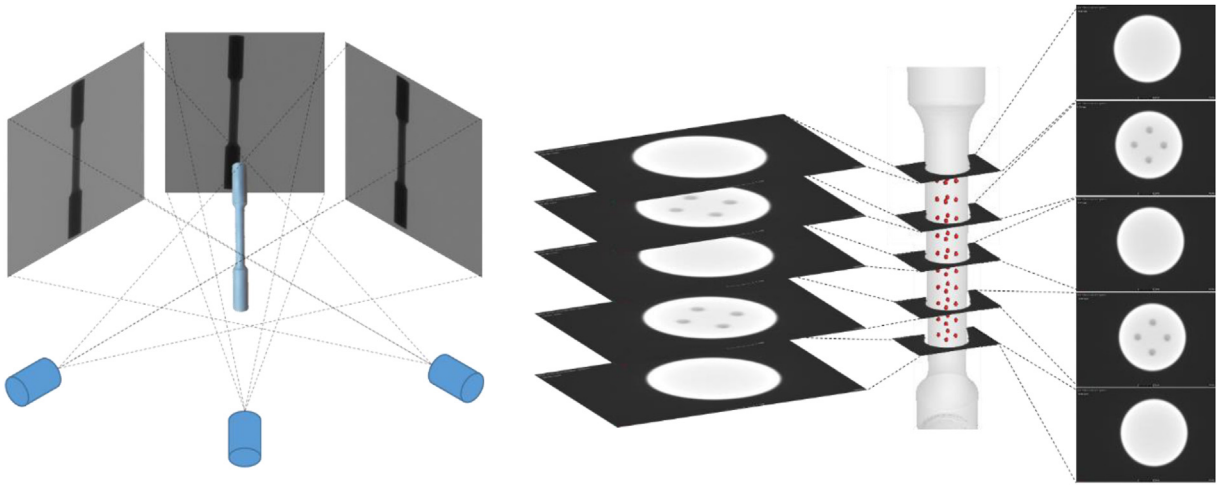

Fig. 2 – Scheme of the XRCT scanning process.

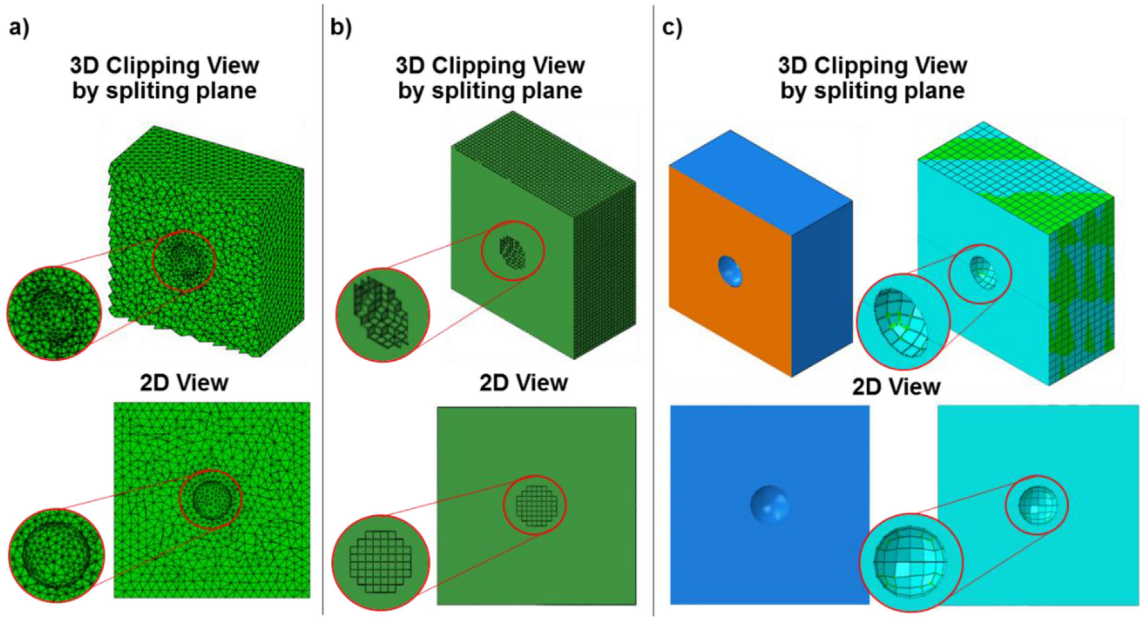

Fig. 3 – Meshing techniques from XRCT data, a) with tetrahedral elements, b) with hexahedral elements and c) with CAD obtained by reverse engineering techniques.

complex shapes of voids, second-order tetrahedral meshing was adopted, increasing number of elements around boundaries of voids and minimizing element sizes in these areas. The number of elements and nodes for each specimen were in ranges of 0.5–1.7e^6 and 0.8–2.4e^6, respectively. The minimum element volume achieved is approximately 8.6e^{-7} mm^3.

2.4.2. *FEM modelling*

Once the XRCT analysis and the meshing strategy have been defined, the FEM modeling for the virtual tensile test was programmed. For this purpose, ABAQUS 6.14 software was utilized, selecting C3D10 M as the element type. For the definition of mechanical material properties, both, literature and experimental data were used. On the one hand, the Poisson's ratio was set at 0.33 according to Ref. [51]. Density was set as 2.7 g cm^{-3} [52]. On the other hand, the elastic-plastic behavior was calibrated according to the experimental tensile tests of Specimen O1 (Section 3.2). Finally, the failure was established based on ductile damage theory of continuum damage mechanics [53]. This phenomenological model focuses on void nucleation, growth and coalescence, matching the fracture mechanism observed in the study. Therefore, damage initiation and evolution could be defined.

According to the adopted approach, damage initiation was reached when Eq. (1) [53,54] was met:

$$\omega_D = \int \frac{d\bar{\varepsilon}^{pl}}{\bar{\varepsilon}_D^{pl}(\eta, \Theta, \dot{\bar{\varepsilon}}^{pl})} = 1 \quad (1)$$

where state variable (ω_D) indicates the damage initiation as function of plastic deformation. $\bar{\varepsilon}^{pl}$ refers to the equivalent plastic strain. $\bar{\varepsilon}_D^{pl}$ concerns to this variable at the onset of damage, which is defined dependent on the stress triaxiality (η), Lode angle (Θ) [54] and equivalent plastic strain rate ($\dot{\bar{\varepsilon}}^{pl}$).

Damage evolution was described by the overall damage variable (D), which indicates the progressive degradation of the material stiffness, leading to the final failure. The evolution of the damage variable ($\dot{D}$) was assumed linear according to Eq. (2). Finally, when the damage variable (D) reached the unity, defined as the maximum degradation value, the element was removed.

$$\dot{D} = \frac{\dot{\bar{u}}^{pl}}{\bar{u}_f^{pl}} \quad (2)$$

where $\bar{u}_f^{pl}$ refers to the equivalent plastic displacement at failure.

Apart from that, the boundary conditions were defined according to the experimental tensile test conducted. At the base of the model, both displacement and rotation on the z-axis were restricted, while continuous displacement of the upper face of the model was imposed.

The XRCT-based FEM model was validated by means of experimental tensile tests. For that purpose, an Instron 8801 servohydraulic fatigue testing system (Instron, Norwood, MA, USA) was used. These tests were conducted using a speed of 0.008 s^{-1} [55,56], according to ASTM E8/E8M.

The workflow of the described methodology is summarized in Fig. 4.

3. Results and discussion

3.1. *XRCT porosity analysis*

In order to assure the appearance of designed porosity and estimate the presence of non-defined porosity, the XRCT porosity analysis was carried out. As a result, the porosity percentage of

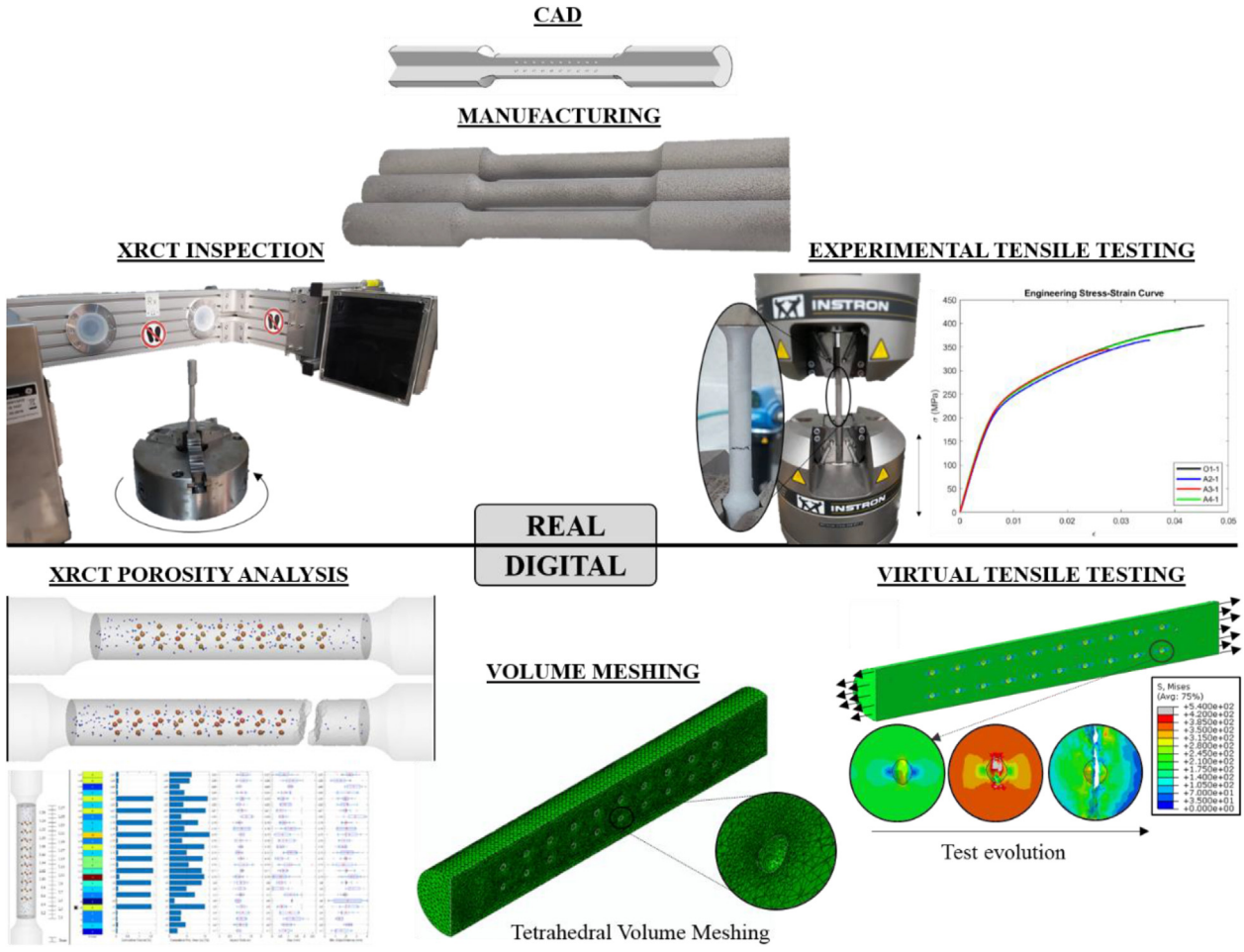

Fig. 4 – Workflow of the proposed methodology.

each as-built specimen is presented in Table 4. It reveals that detected porosity differs from the designed porosity.

In addition, results obtained for each type of sample are shown in Fig. 5. Both, as-built and fractured specimens are displayed. The volume of each detected void is illustrated by means of a color-bar.

According to the obtained results, all designed voids were detected for A2, A3, A4, B2 and B3 specimens. However, for C2 and C3 specimens, some of them were not detected, possibly due to their small size. Apart from that, the presence of non-defined porosity is significant in all specimens.

Therefore, results presented in Table 4 and Fig. 5 suggest that a depth analysis is required in order to estimate the achieved porosity and the influence of voids on the mechanical behavior of each specimen. To this end, different porosity features were defined for the study:

- Firstly, the volume of each detected void is considered.
- For the shape analysis, two parameters were defined:
  - o Projected area on the plane normal to the applied load.
  - o Aspect ratio, which is defined by using the sizes of the bounding box surrounding the detected void in the co-ordinate system. This parameter is established as the ratio between the half of the maximum size of the bounding box on the cross-sectional plane (a) and the half size of the box on Z axis (c).
- For the void location, spacing and distance to the edge, the following parameters were defined:

Table 4 – Porosity percentage of each as-built AlSi10Mg specimen with artificial porosity.

Porosity percentage [%]								
Specimen #	O1	A2	A3	A4	B2	B3	C2	C3
1	0.077	0.546	0.686	0.587	0.255	0.240	0.063	0.054
2	0.109	0.572	0.599	0.573	0.253	0.355	0.030	0.107
3	0.093	0.608	0.565	0.605	0.254	0.304	0.039	0.032
Mean value (μ)	0.093	0.575	0.617	0.588	0.254	0.300	0.044	0.064
Standard deviation (σ)	0.016	0.031	0.062	0.016	0.001	0.058	0.017	0.039

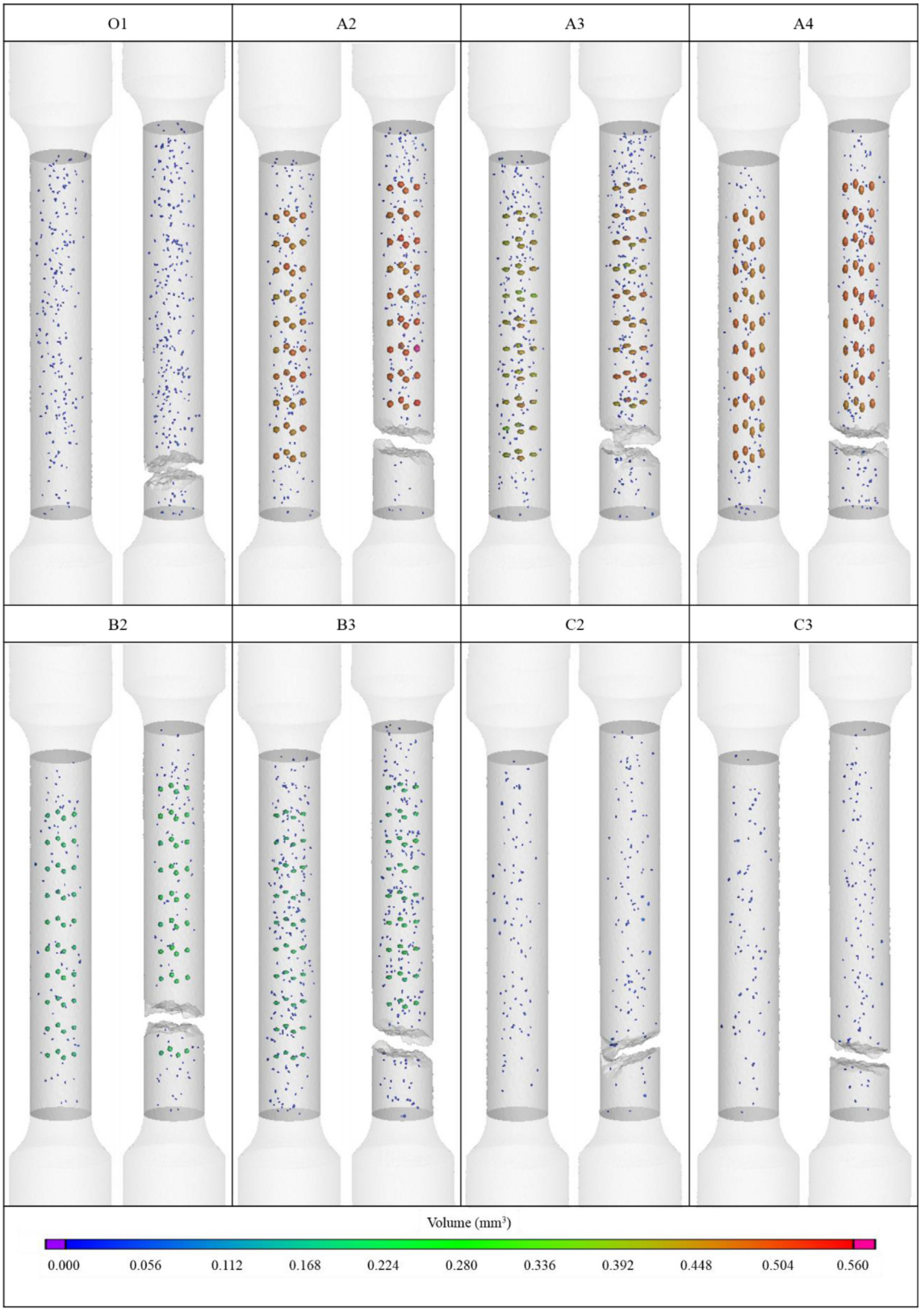

Fig. 5 – XRCT porosity analysis in the region of interest of each AlSi10Mg specimen. As-built and fractured samples are displayed.

- o Gap, which refers to the minimum length between the surface of the circumscribed spheres of the nearest pores.
- o Minimum edge distance, which indicates the smallest distance between the surface of the pore and the surface of the specimen.

Statistical results of these defined features for each type of specimen are presented in Fig. 6.

As depicted in Fig. 6, O1 specimens show voids with mean volumes of 0.014 mm^3 and a standard deviation of 0.006 mm^3. Since these specimens were defined without voids, these values reveal the presence of non-defined voids due to the manufacturing process. Focusing on shape results, mean projected area is around 0.089 mm^2, with all of its values below 0.209 mm^2. The mean aspect ratio is 7% higher than the unity, with an interquartile range of 0.833–1.248. It shows the considerable predominance of nearly spherical shape of the detected voids. Regarding the void location and spacing, gap reveals mean and standard deviation results of 0.780 ± 0.459 mm. These results for minimum edge distance of voids are around 2.179 ± 0.888 mm. As a result of the appearance of these non-defined voids and its features, the mechanical behavior of each specimen is affected, as shown in the following section (Section 3.2).

Focusing on volume statistics, the presence of porous with lower volumes than defined decrease the results obtained, especially for A2, A3, A4, B2 and B3 specimens. The volume established per void of A2, A3 and A4 is 0.524 mm^3, while the results obtained reveal mean and standard deviation values of 0.136 ± 0.200 mm^3, 0.070 ± 0.142 mm^3, 0.194 ± 0.228 mm^3, respectively. In addition, interquartile ranges of 0.011–0.432 mm^3, 0.011–0.020 mm^3 and 0.012–0.479 mm^3 were achieved. These results highlight an increase in the amount of non-defined voids in A3 specimens compared to A2 and A4 samples. Apart from that, maximum values report a decrease of 0.687%, 8.136% and 2.215% from design, according to the established order. Thus, defined voids show a noticeable reduction in volume, especially for oblate shapes followed by prolate shapes. This is probably caused by manufacturing process and the increased downskin areas in oblate shapes.

B2 and B3 specimens share void volumes of 0.268 mm^3 by design. B2 samples show statistics with average of 0.084 ± 0.090 mm^3 for mean and standard deviation. However, B3 specimens show a mean value of 0.046 mm^3 and a deviation of 0.068 mm^3. Thus, both type of specimens suffer the appearance of non-defined voids with sizes lower than designed. These effect exhibits a marked increase in B3 samples. Interquartile ranges of B2 specimens show 0.012–0.192 mm^3, while B3 samples decrease to 0.011–0.023 mm^3.

Finally, C2 and C3 specimens show volumes with a mean value of 0.014 mm^3 and deviations between 0.006 and 0.007 mm^3, respectively. 0.014 mm^3 was established as the volume of voids by design. Hence, the sizes of the voids detected in these samples, both designed and non-designed, are comparable. Note that as depicted, non-defined voids in samples O1, C2 and C3 present similar statistics.

3.1.1. *Void shape analysis*

The indicators selected to analyze the shape of voids also show the aforementioned outcomes. As shown in Fig. 6, all projected areas are below 1.2 mm^2 and most of results for aspect ratio are in range of 0.5–2. Focusing on projected areas, apart from C2 samples, non-defined voids decrease mean values compared to designed ones. A2, A3, A4, B2 and B3 specimens show a mean value decrease of 0.510, 1.037, 0.241, 0.278 and 0.629 mm^2, respectively. Associate deviations of 0.308, 0.322, 0.219, 0.179 and 0.188 mm^2 are reported. As demonstrated, the larger the defined projected areas, the greater the differences obtained. This effect is promoted by the reduced projected areas of non-defined voids in comparison with designed ones with highest projected areas. Thus, A3 samples, followed by B3, presents the main differences due to both, the increased of those non-defined voids and the difference between projected areas of defined and non-defined voids. In agreement, A2 samples also shown a considerable decrease with respect to the rest of specimens. Although different shapes are defined, the similar projected areas defined for A4 and B2 samples provoke comparable statistics. Instead, C2 samples present a mean value increase of 0.012 mm^2 with a deviation of 0.022 mm^2, while C3 results decrease 0.026 mm^2 with deviation of 0.027 mm^2. As indicated, median obtained for these specimens are 0.080 mm^2, with interquartile ranges of 0.068–0.096 and 0.072–0.096 mm^2, respectively. Hence, the results are close in both cases, as previously observed.

For A2, B2 and C2, the defined aspect ratio is the unity, which reveal spherical void shape. The results obtained show a mean value increase around 9%, 11% and 8% with deviations of 0.236, 0.262 and 0.308, respectively. The shape of voids defined by design for A3, B3 and C3 is an oblate ellipsoid with aspect ratio of 2. Nonetheless, the statistical results obtained by the analysis reveal a strong influence of non-defined voids with aspect ratios lower than defined. This fact promotes a decrease of the mean value of the aspect ratios of about 40%, 41% and 46% with deviations of 0.371, 0.368 and 0.300, respectively. This effect is also shown in A4 specimens. They were defined with prolate shapes and 0.5 aspect ratios, while the obtained results were averaged in 79% increase. As a result, 0.896 ± 0.316 were obtained for the mean value and standard deviation. Finally, the median values obtained for each specimen approximate to the unity. The median value of A4 is notable for its 20% decrease against the 10–12% increase of the A3 and B3 samples with oblate shapes. B2 samples also report an increase of 8%. Hence, although non-defined voids show different aspect ratios from 0.5 to 3, the majority of non-defined voids shows aspects ratios closed to the unity, revealing nearly spherical shapes.

3.1.2. *Void location analysis*

Regarding the location and spacing of voids, gap results reveal a decreasing statistics from the designed. Each type of specimen presented shows an average gap reduction of about 53%, 64%, 59%, 48%, 63%, 58% and 63%, according to the established order. As shown, non-defined voids reduce the minimum distance between the nearest voids due to their appearance at undesired positions. In fact, main differences are shown by specimens with oblate designed voids, where the number of undefined voids increases. Negative values should not be confused, they are obtained owing to the very nature of the parameter definition.

Finally, the statistics of the minimum edge distance seem to be more balanced than the previous parameters, at least

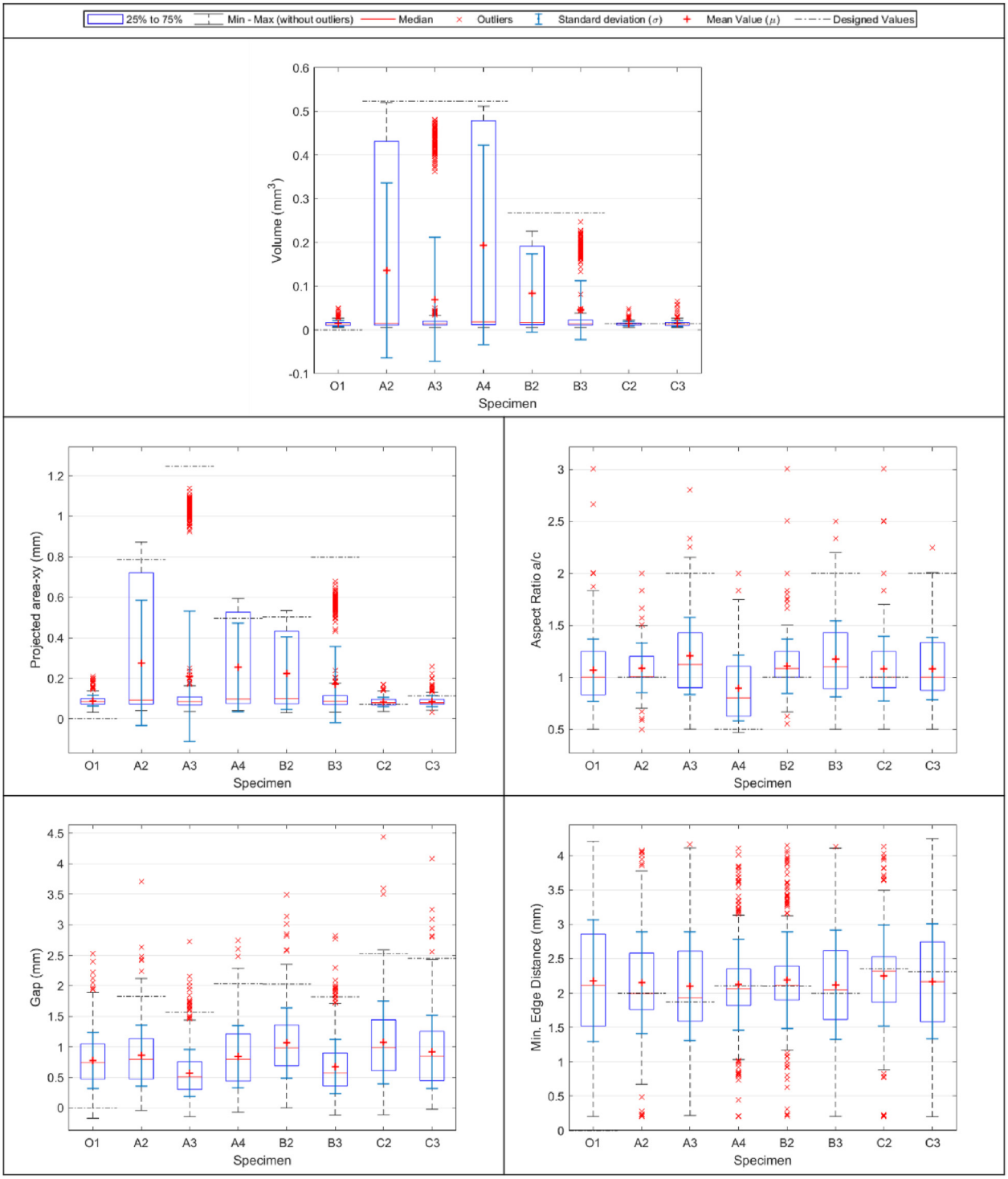

Fig. 6 – Statistics of the XRCT porosity analysis of each as-built AlSi10Mg specimen. Results in comparison with the designed values are displayed.

focusing on median values. Differences of around 1%, 3%, 2%, 1%, 2%, 2% and 6% were obtained with respect to the values designed for each one. Nevertheless, focusing on spread of the obtained values, interquartile ranges show 0.821, 1.022, 0.530, 0.494, 1.003, 0.663 and 1.161 mm, respectively. Thus, specimens with oblate defined voids exhibit the highest ranges due to the increased presence of non-defined voids. As stated above, non-defined voids at unwanted locations promote the differences between designed and manufactured samples in porosity statistics. Minimum edge distance results reveal these effects through the spread statistics.

In order to estimate the influence of the porosity features defined on the mechanical failure of each specimen, the analysis was detailed by specimen sectioning at each 2 mm in

Z-axis. As an example, results obtained for A2 specimen are illustrated in Fig. 7.

As depicted in Fig. 7, the statistical analysis of each defined feature presents the worst results at those levels at which designed voids were detected. Hence, the fracture of the specimen is prone to take place at that section. In addition, the considerable amount of non-defined voids detected through this specimen has a strong influence on the statistical analysis per level. The increases in void volume percentage, projected area percentage and aspect ratio, as well as the decrease in pore spacing and minimum edge distance, are indicators of the fracture occurrence probability at that section. Nonetheless, the homogeneous distribution of designed voids and the highly amount of non-defined voids, results in similar statistics per level, which complicate the fracture level estimation. Thus, FEM analysis is preferable for prediction due to it takes into account all void features. Apart from that, it is worth mentioning that non-detected defects possibly influences the section at which fracture take place [57,58]. The results obtained for all the specimens are presented in Figs. A–H (Appendix).

3.2. *Experimental tensile tests results*

From the experimental tensile tests carried out for AlSi10Mg specimens, the Engineering Stress-Strain curves of each specimen were obtained. As a result, these curves for the first specimen without defined porosity (type O1), as well as specimens of types A2, A3 and A4 are presented in Fig. 8.

According to Fig. 8, the performance of the majority of specimens follows similar trajectories; however, some specimens reach the failure earlier than others. Thus, the main difference is explained by means of ultimate tensile strengths and elongations at fracture (see Table 5). The mean value and standard deviation are depicted, for both, experimental test and FEA. It is worth mentioning that for both, experimental tensile tests and XRCT-based FEM models, 3 samples of each type have been considered.

Results show that a degree of consistency between ultimate tensile strength and elongation at fracture is demonstrated. In addition, due to the considerable amount of non-defined voids in all specimens, the effect on failure occurrence is mitigated between samples. Nonetheless, focusing on O1 specimens, the

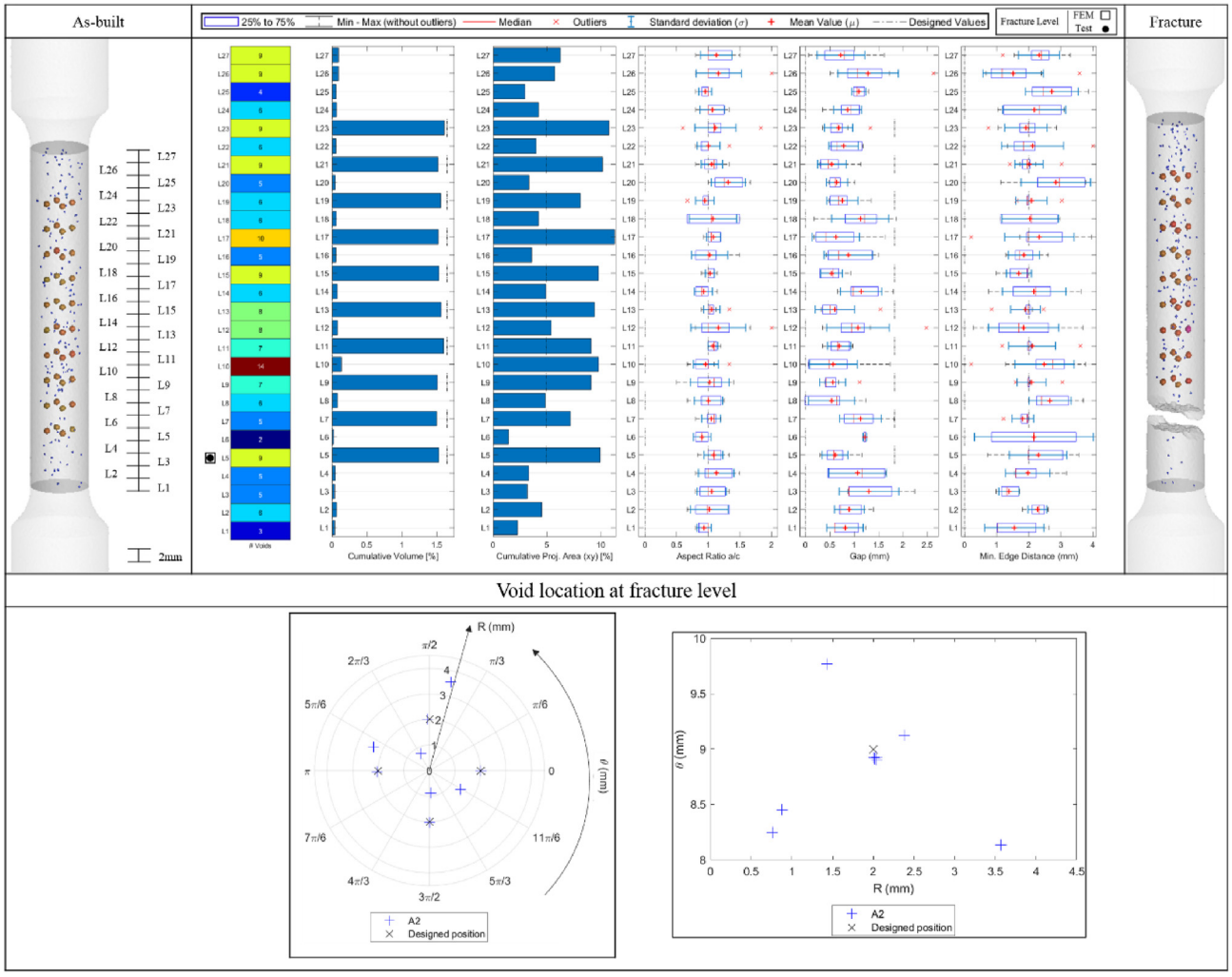

Fig. 7 – Statistics of the XRCT porosity analysis of third specimen of A2-type sample. Results of each section are displayed focusing on the fracture level.

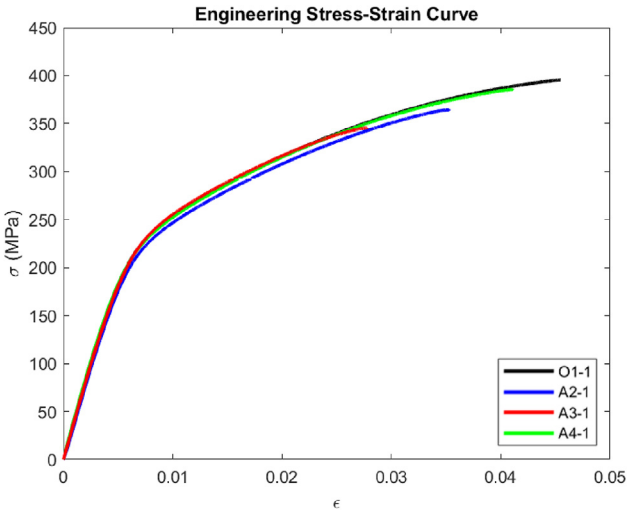

Fig. 8 – Engineering Stress-Strain curve of first specimens of type O1, A2, A3 and A4.

appearance of non-defined voids affect their performance. In fact, C2 specimens increase the elongation statistics of O1 by 0.11% on average, while C3 samples exhibit a mean decrease of only 0.06%. Hence, these results are in accordance with porosity analysis carried out in previous section, where the porosity features showed similar results on these samples. As mentioned, the porosity statistics of C2 are slightly better than those of C3, which in turn are better than those of O1, especially based on projected area, gap and minimum edge distance. In addition, porosity percentages correlate with these results by increasing from 0.044% to 0.064% and 0.093% on average, respectively.

3.2.1. *Influence of the void size on mechanical properties*
Regarding relationship between the void size and mechanical behavior, it could be concluded that reducing the size of defined voids while keeping the designed shape promote the delay of failure, as demonstrated by A2, B2 and C2 (defined voids with spherical shape) specimens and A3, B3 and C3 (defined voids with oblate shape) specimens. For spherical shapes, samples demonstrate that a reduction of 48.80% (A2–B2) and 97.30% (A2–C2) in theoretical volumes provides an increase of elongation at fracture by approximate 9.71% and 28.86% on average, respectively. In contrast, the same reduction for oblate shapes (A3–B3 and A3–C3) shows an average increase of 17.33% and 56.68% of elongations achieved. Thus, the reduction of void size has an impressive effect on specimen behavior and failure. In addition, shape effect is needed to be considered since oblate voids show nearly the double effect on elongation than spherical voids with the same volume reduction.

3.2.2. *Influence of the void shape on mechanical properties*
Regarding the shape analysis, varying the shape of defined voids concerns both, strength and elongation. Defined voids with prolate shapes extend the final failure, followed by spherical shapes and, finally, oblate shapes. This is caused by the increase of stress concentration around that voids, in that order. This effect is exhibited by comparing A4, A2 and A3 specimens due to the fact that all of defined voids were designed with the same volume, while shapes of voids match the previous description, respectively. Hence, A3 specimens show an elongation reduction by approximate 20% on average from A2 samples, while increase the aspect ratio by 2. On the other hand, A4 samples reveal the opposite effect, with a 20% increase of elongation and aspect ratio reduction to the half of the defined for the spherical shapes.

Outcomes of pairs B2–B3 and C2–C3 replicate the mentioned effect, but the decrease in elongations achieved is reduced to 15% and 4%, for each case.

Thus, volume and shape of voids have distinct effects on the mechanical behavior and failure of the component with means that they should be analyzed independently.

3.2.3. *Influence of the void location on mechanical properties*
According to the design, defined voids are located at the same place. Thus, void size and shape affect their location analysis regarding to gap between voids and minimum edge distance. In that context, trends to small sizes and prolate shapes induce better location results and also promote the delay of failure.

As expected, specimens defined with oblate voids, especially A3 and B3 samples, present the lowest values for void location analysis, mainly in the gap indicator. In addition, the considerable increase of non-defined voids in these samples affects their statistics. According to that, these specimens reach the failure earlier than others, while, for instance, A4 samples reveal the opposite effect owing to both, defined voids and a reduction of non-defined voids.

Therefore, a decrease of these porosity features, together with the other studied aspects, encourages a reduction of the resistant section, promoting stress concentration and, finally, coalescence between voids.

Images of the fracture surfaces of each specimen are displayed in Fig. I (Appendix). As depicted, these specimens present a moderately ductile fracture with typical cup-and-

Table 5 – Ultimate tensile strength and elongation at fracture of AlSi10Mg specimens.

	Tensile test (Experimental)		Tensile test (Simulation)		Error	
Specimens	σ_{UTS} [MPa]	A_t [%]	σ_{UTS} [MPa]	A_t [%]	σ_{UTS} [%]	A_t [%]
O1	397 ± 2	4.40 ± 0.16	384 ± 3	4.19 ± 0.12	3.36	4.67
A2	370 ± 7	3.50 ± 0.04	364 ± 2	3.43 ± 0.11	1.52	1.91
A3	342 ± 3	2.77 ± 0.02	340 ± 2	2.81 ± 0.06	0.69	1.27
A4	389 ± 5	4.19 ± 0.07	381 ± 3	4.04 ± 0.10	2.09	3.63
B2	382 ± 6	3.84 ± 0.06	383 ± 2	3.98 ± 0.06	0.29	3.52
B3	363 ± 5	3.25 ± 0.05	359 ± 4	3.25 ± 0.05	1.10	0.04
C2	401 ± 1	4.51 ± 0.25	389 ± 3	4.27 ± 0.15	3.14	5.17
C3	397 ± 2	4.34 ± 0.10	387 ± 4	4.15 ± 0.17	2.61	4.33

cone shape. The flat shape at distance to the edge diameter is commonly accomplished by the void coalescence in plane normal to the applied load. In contrast, cone shape is produced by the shear stresses. Accordingly, the onset of fracture is located on that plane normal to the applied load.

3.3. *Virtual tensile test results by means of FEM analysis*

To estimate the behavior and failure of each specimen with respect to the porosity analysis performed, an XRCT-based

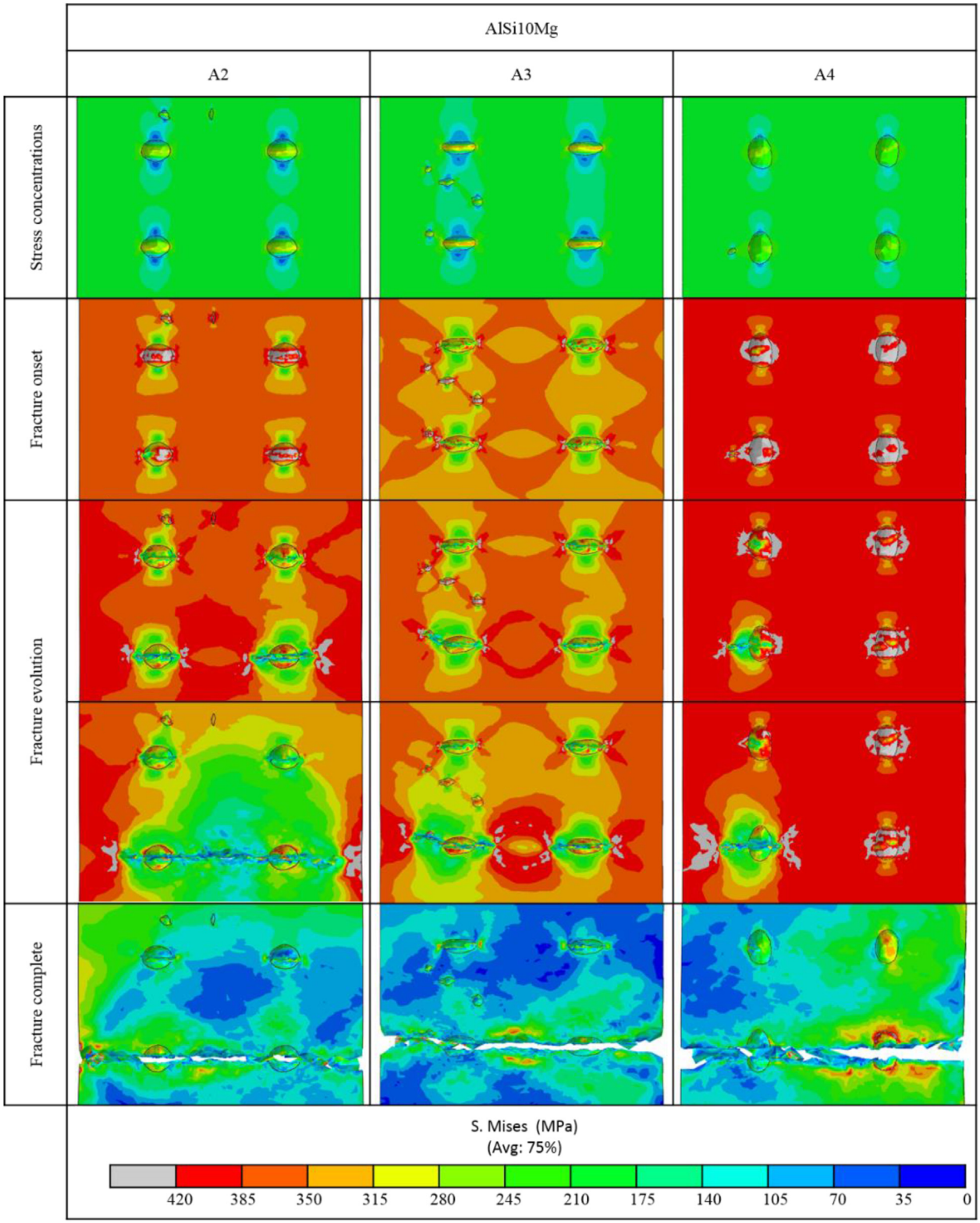

Fig. 9 – XRCT-based FEM results at five different stages for first samples of A2, A3 and A4.

FEM was carried out for each specimen including repetitions. In order to analyze the effect of voids on stress concentration, behavior and final fracture, simulation of A2, A3 and A4 samples are displayed in Fig. 9.

According to results presented in Fig. 9, stress distribution around voids depends mainly on the loading direction. As depicted, when loads are applied in vertical direction, the maximum stress is located around voids equator, whilst minimum stresses are generated around void poles. This effect is caused by the triaxial stress state produced around free surfaces of voids, which increases as the angle between the normal of the defect surface and the loading direction rises. Thus, the growth arises from defect surfaces perpendicular to the applied load (poles of nearly spherical or ellipsoidal voids) to parallel surfaces (equator of designed voids). In addition, the shape of the pores affects the stress distribution around voids. Oblate and irregular geometries increase the stress values, while prolate shapes decrease these values. Hence, pronounced curvatures of defect surfaces, mainly located around void equator, promote the increase of the stress concentration. As consequence of the material ductility, when local stresses around voids exceeds yield stress, plastic deformation takes place, decreasing sharp of voids and, therefore, relaxing stresses. Thus, void growth tends to prolate shapes, reducing aspect ratios as the test progress. Finally, the onset of fracture is located at voids equator, where stress exceeds ultimate tensile strength of material. The crack growth is driven by reduction of material area, promoting the coalescence between voids. In this framework, the gap between voids and the minimum edge distance encourage the void coalescence and, thus, the earlier failure of the component.

The results obtained by the XRCT-based FEM analysis are correlated with experimental results. Both, ultimate tensile strength and elongation at fracture were summarized in Table 5. Maximum errors of 3.36% and 5.17% are obtained, respectively. As shown, errors increase as elongation increases. Although there are several factors that affect the simulation performance and failure estimation, such as behavior and failure modelling, meshing strategy and mesh quality, this effect is possibly due to the fact that the more the elongation increases (the more the failure is delayed), the smaller the slope of the Stress-Strain curve, showing a growth of strain with nearly constant stress. In addition, these samples present barely necking effect. Hence, this situation complicates the prediction of simulation for failure occurrence, exhibiting an increase of errors for those specimens. Nonetheless, the failure estimation by simulation is consistent for the sample repetitions.

Therefore, the proposed methodology focused on XRCT-based FEM provides reliable results to estimate the specimens behavior according to their detected porosity. Thus, the proposed methodology is considered suitable for predicting the susceptibility to failure related to the different porosity features studied. On the other hand, the fracture level prediction is also analyzed, with 37.5% success rate. The lack of accuracy in the prediction of the failure level is possibly caused by the homogeneous distribution of designed voids and the highly amount of non-defined voids, which results in similar porosity features per level. As stated above, this effect, together with non-detected defects, complicates an accurately fracture level estimation. Nonetheless, the fracture level prediction by XRCT-based FEM presents a consistency with XRCT porosity analysis.

4. Conclusions

In the present work, a methodology to estimate the influence of porosity on the mechanical behavior and failure of AlSi10Mg L-PBF specimens by means of XRCT-based FEM is presented. The results of the proposed methodology reveal considerable reliability. FEM results pointed out that the presence of porosity defects concentrates stresses around them and promotes the final failure driven by both void growth and coalescence. Void features, such as void size, shape and location, apart from porosity percentage, are considered to estimate stress concentrations and the failure location.

From the research carried out, the following conclusions can be drawn:

- Voids with higher volumes, irregular shapes, increased aspect ratios and projected areas in the normal plane, just like reduced void spacing and edge distance, promote the earlier failure of the components.
- Regarding void shapes, varying them from oblate to prolate ellipsoid promotes the delay of failure, considering the loading direction. This effect is also shown for voids with the same shape while reducing their size.
- The proposed XRCT-based FEM provides well-established results to predict ultimate tensile strength and elongation at fracture. Maximum errors of 3.36% and 5.17% were reached, respectively.
- The prediction of the fracture level by XRCT-based FEM demonstrates that accurate results are obtained for only 37.5% of the samples. Possibly underestimation of non-detected defects on the AlSi10Mg specimens plays a major role to predict the fracture level.

For future research, the influence of real porosity commonly appeared during L-PBF-ed parts should be analyzed including gas porosity, keyhole porosity, and lack-of-fusion porosity. Hence, an in-depth analysis of the influence of void location on the stress concentration, void growth and coalescence should be carried out.

Declaration of Competing Interest

The authors declare that they have no known competing financial interests or personal relationships that could have appeared to influence the work reported in this paper.

Acknowledgements

Grant PID2020-118478RB-100 funded by MCIN/AEI/10.13039/501100011033.

Appendix

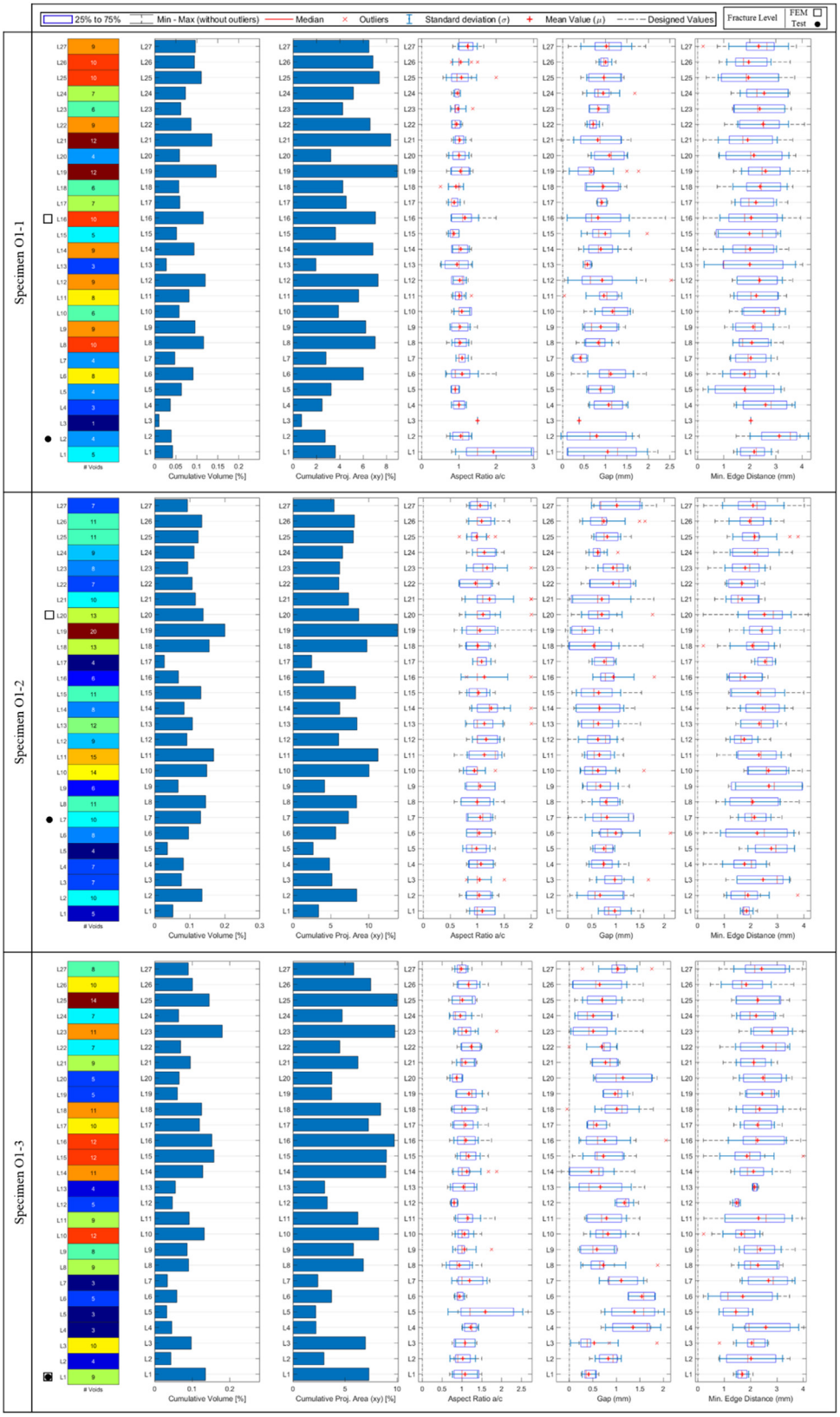

Fig. A – Summary of statistics of the XRCT porosity analysis of O1 specimens. Results of each level are displayed highlighting the fracture level and FEM prediction.

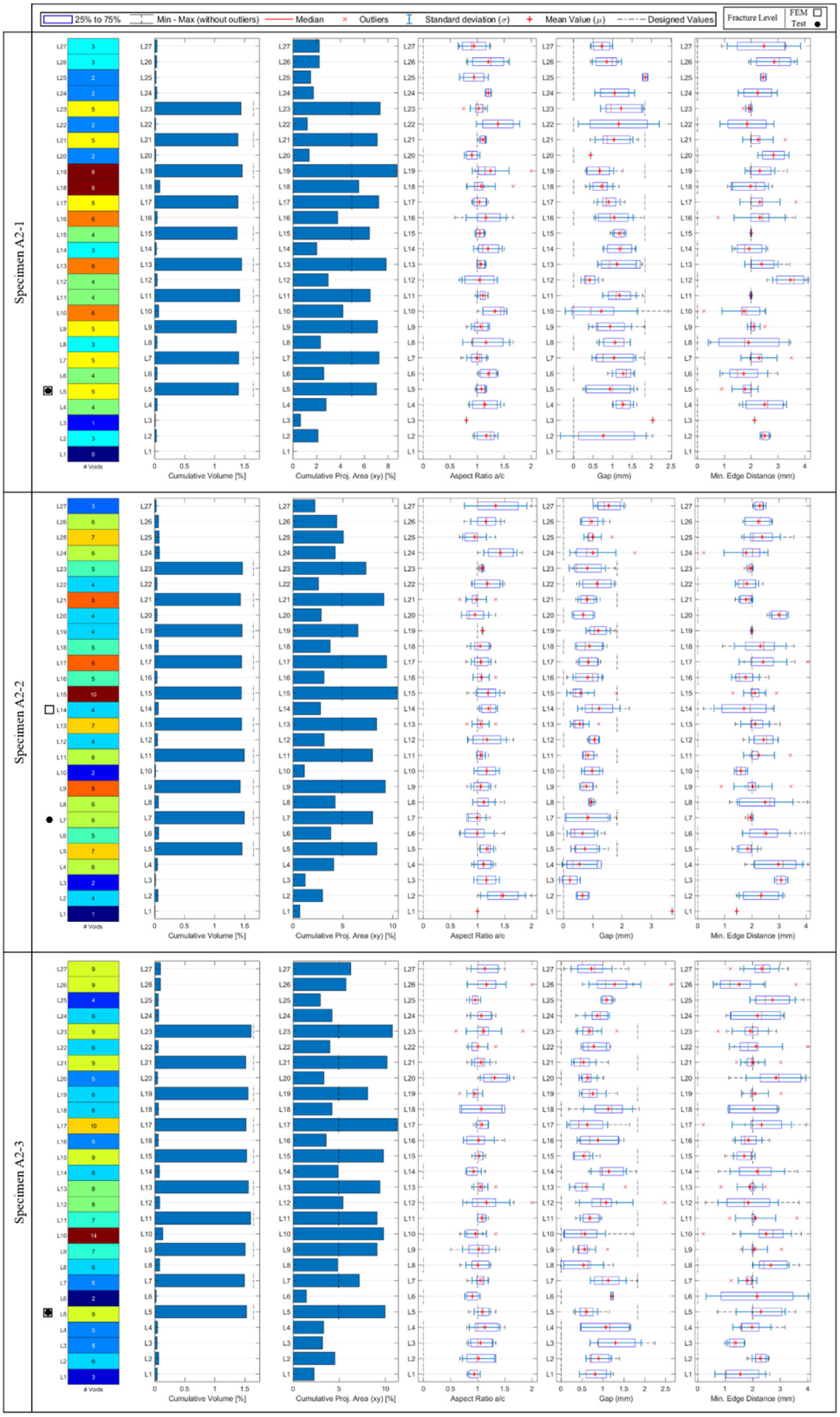

Fig. B – Summary of statistics of the XRCT porosity analysis of A2 specimens. Results of each level are displayed highlighting the fracture level and FEM prediction.

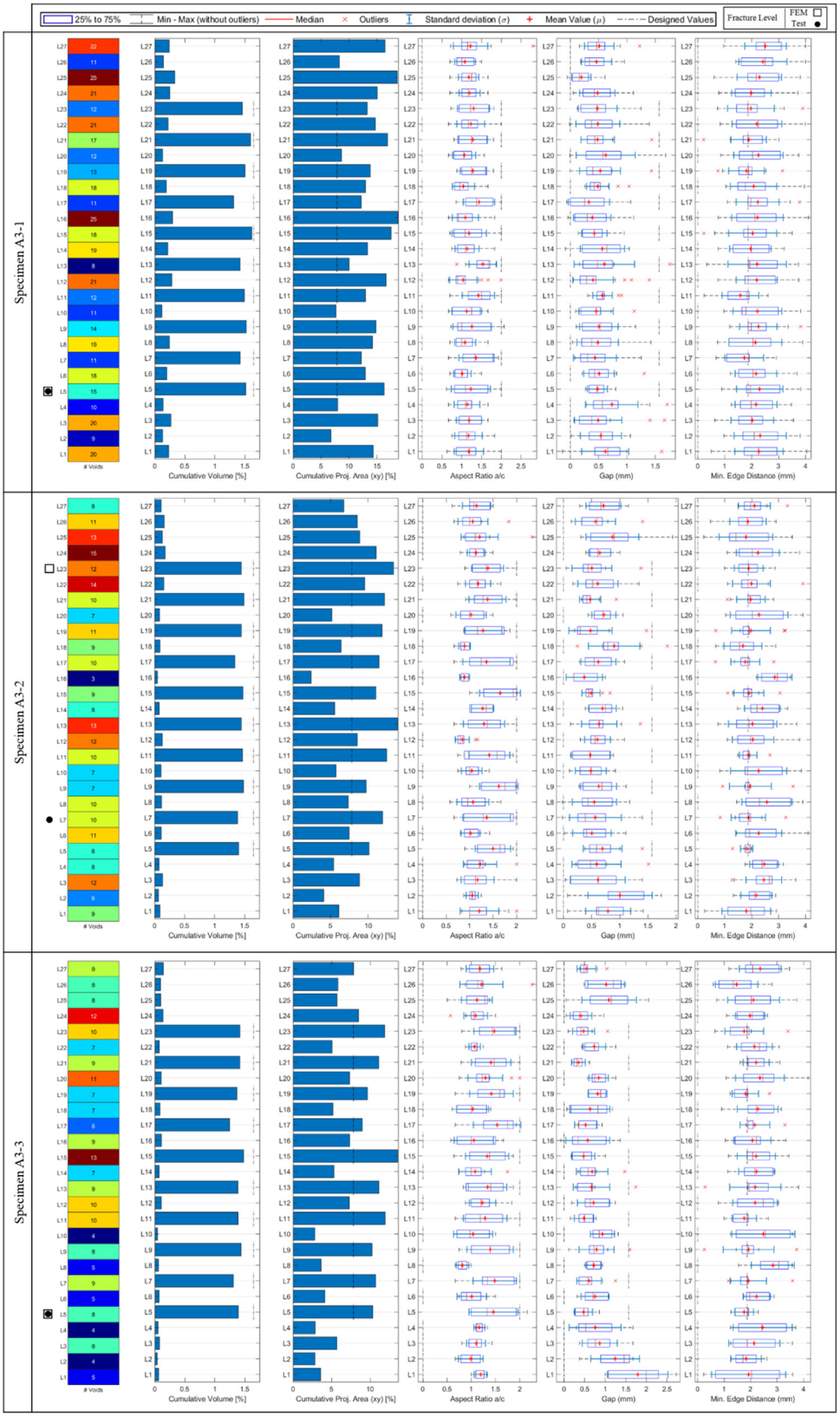

Fig. C – Summary of statistics of the XRCT porosity analysis of A3 specimens. Results of each level are displayed highlighting the fracture level and FEM prediction.

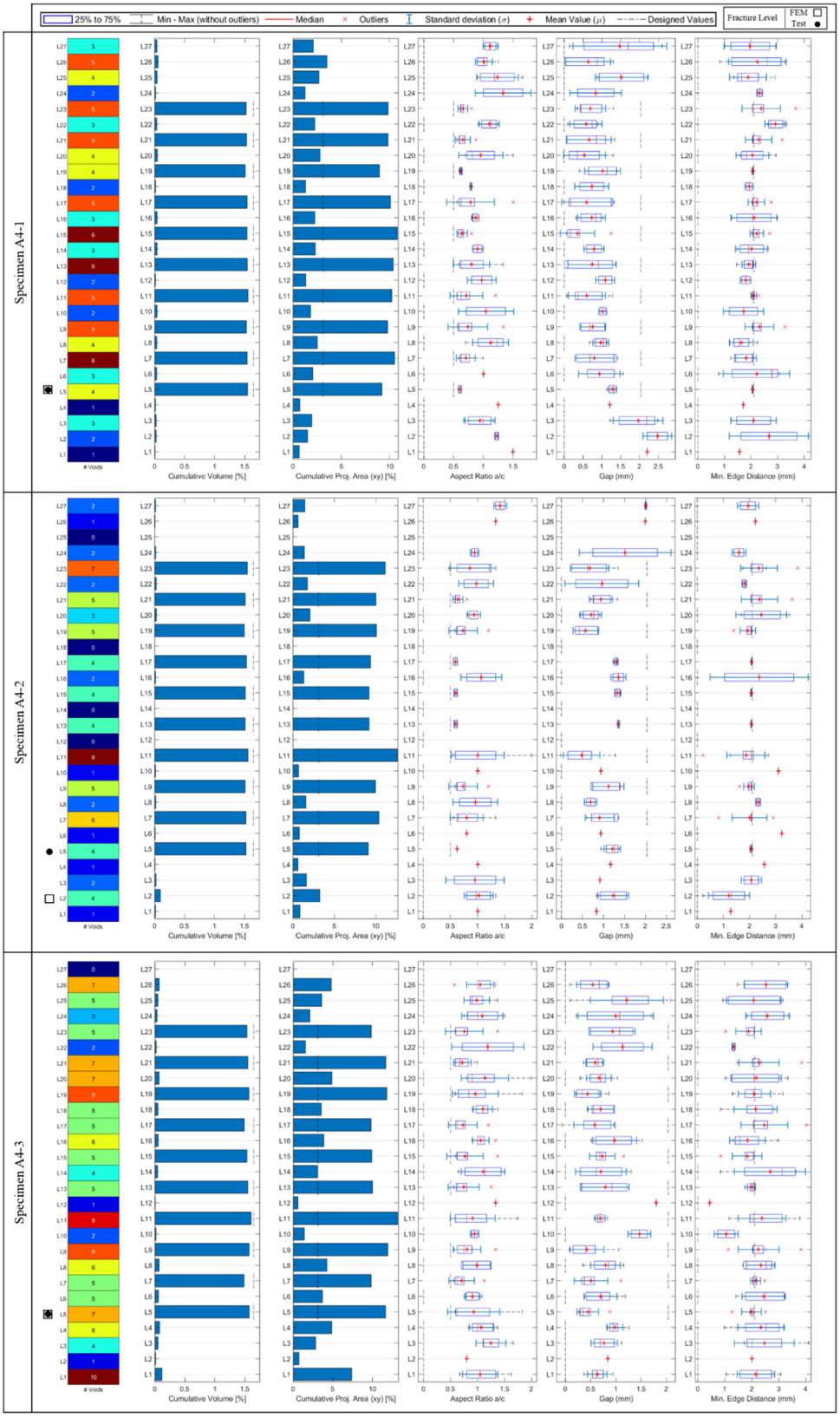

Fig. D – Summary of statistics of the XRCT porosity analysis of A4 specimens. Results of each level are displayed highlighting the fracture level and FEM prediction.

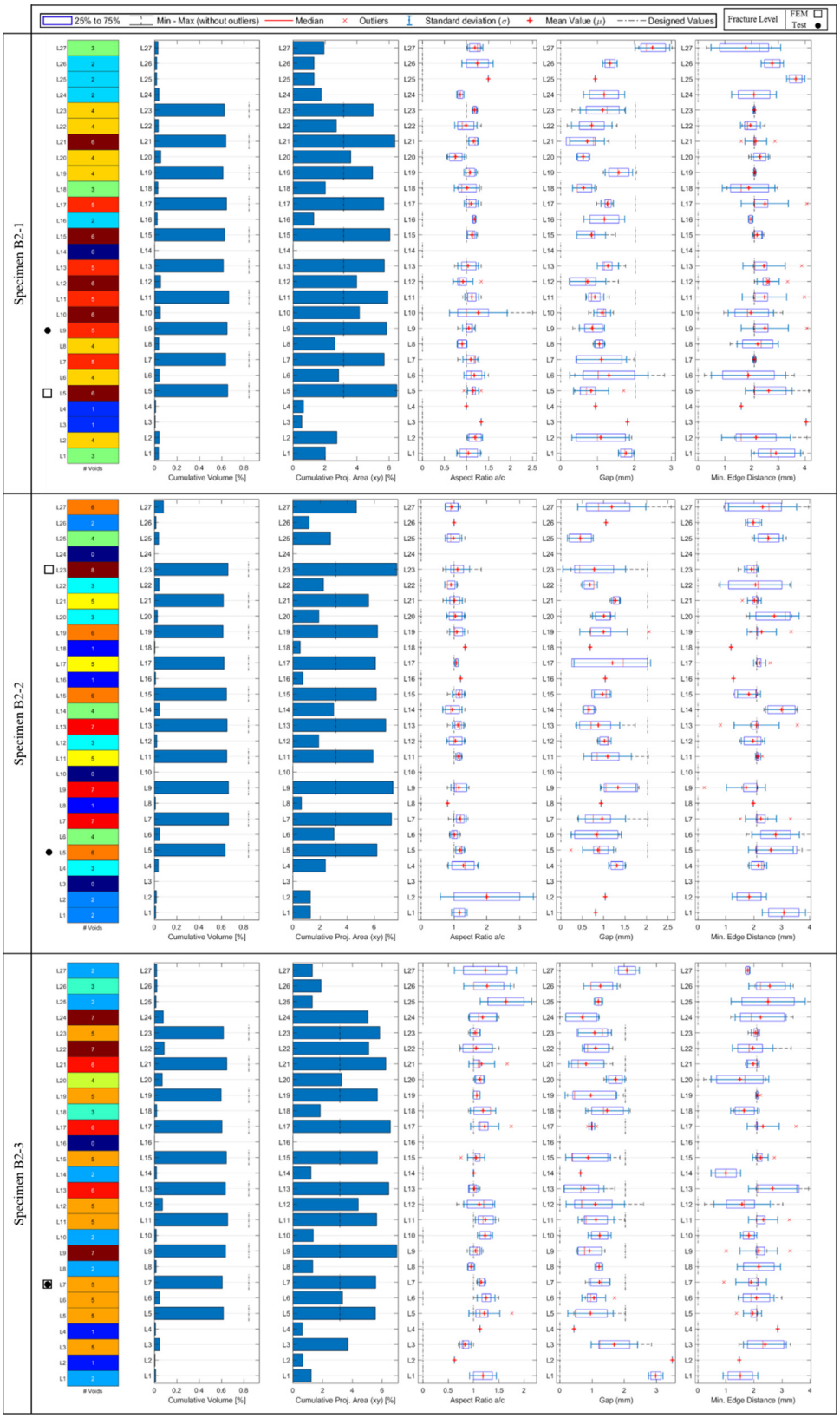

Fig. E – Summary of statistics of the XRCT porosity analysis of B2 specimens. Results of each level are displayed highlighting the fracture level and FEM prediction.

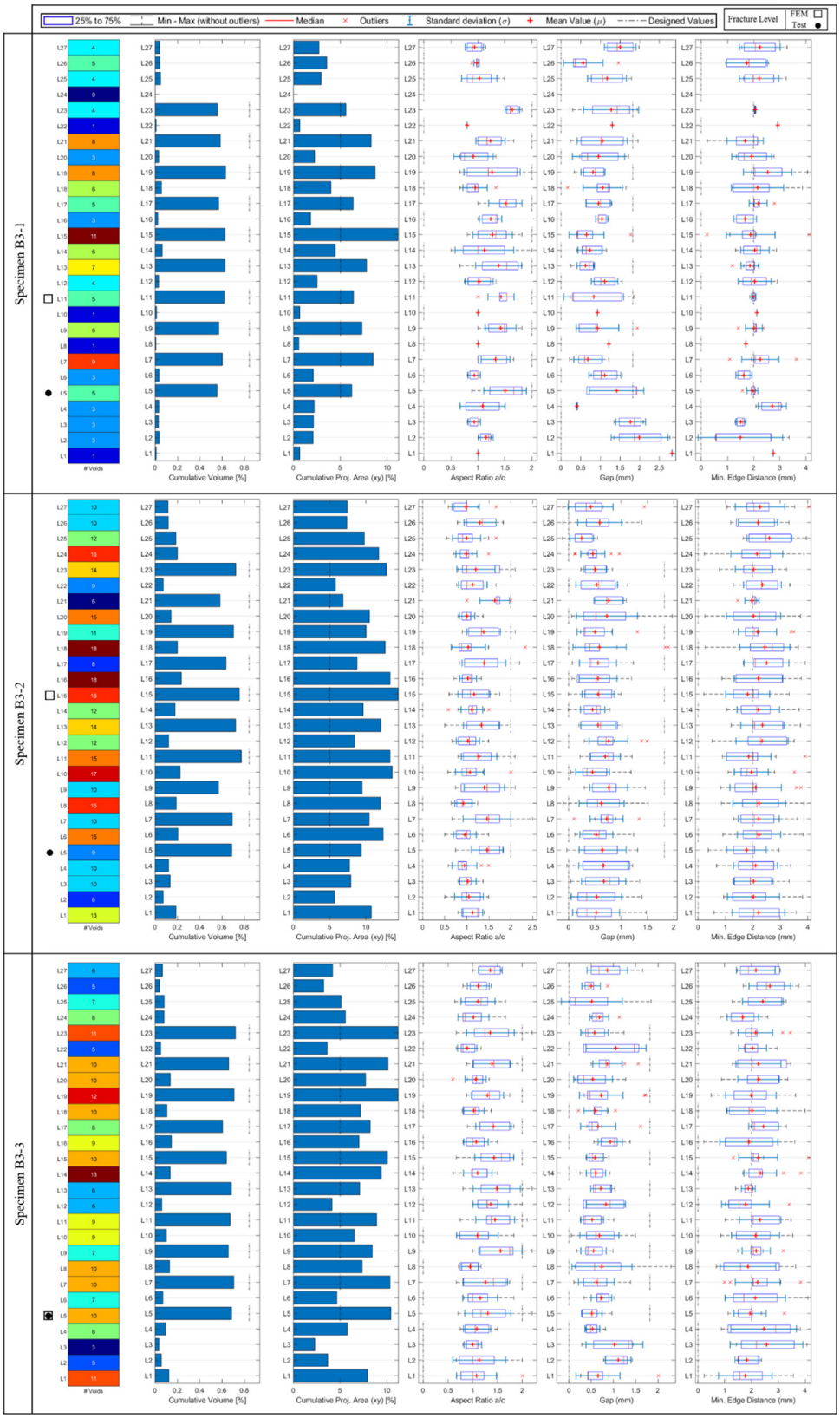

Fig. F – Summary of statistics of the XRCT porosity analysis of B3 specimens. Results of each level are displayed highlighting the fracture level and FEM prediction.

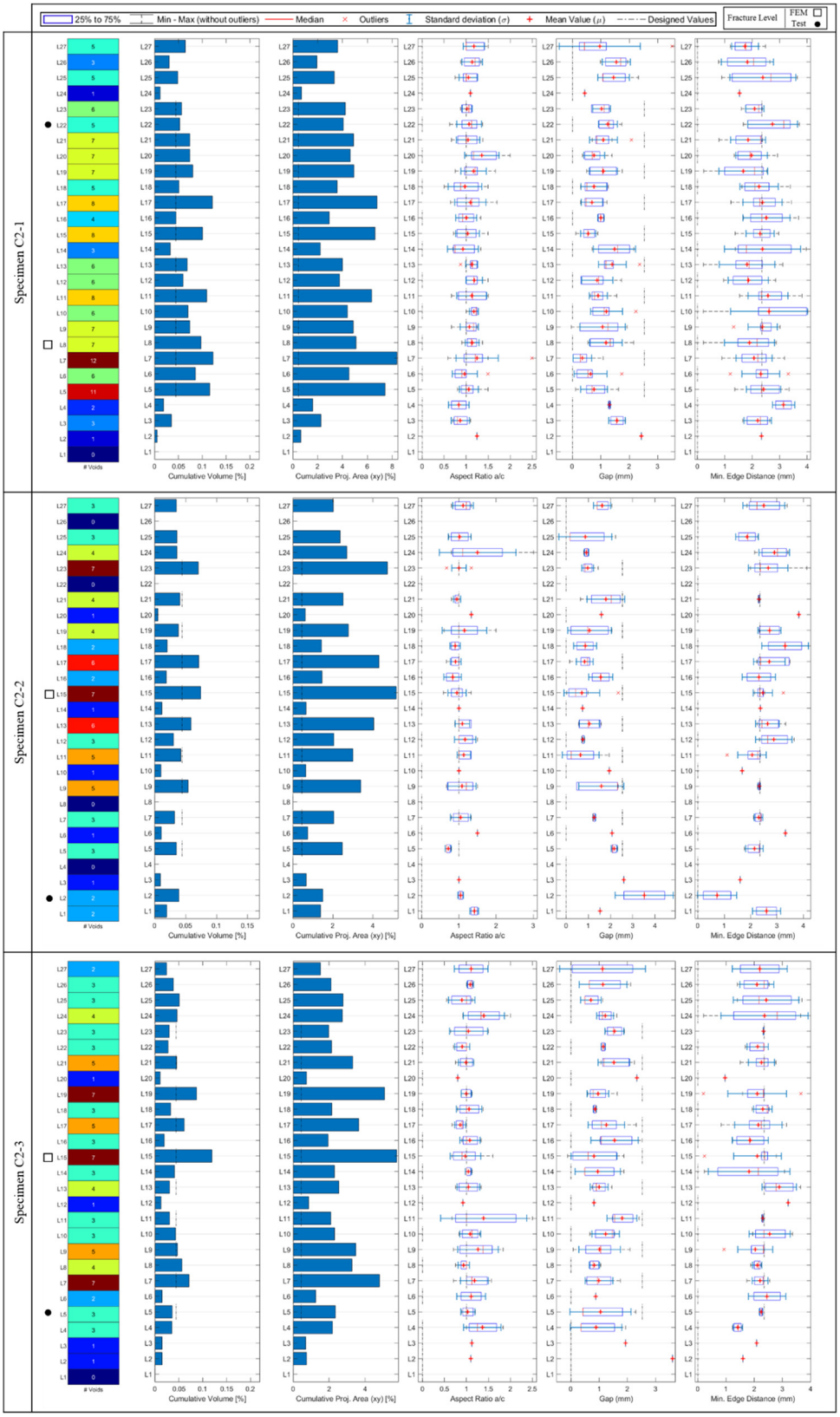

Fig. G – Summary of statistics of the XRCT porosity analysis of C2 specimens. Results of each level are displayed highlighting the fracture level and FEM prediction.

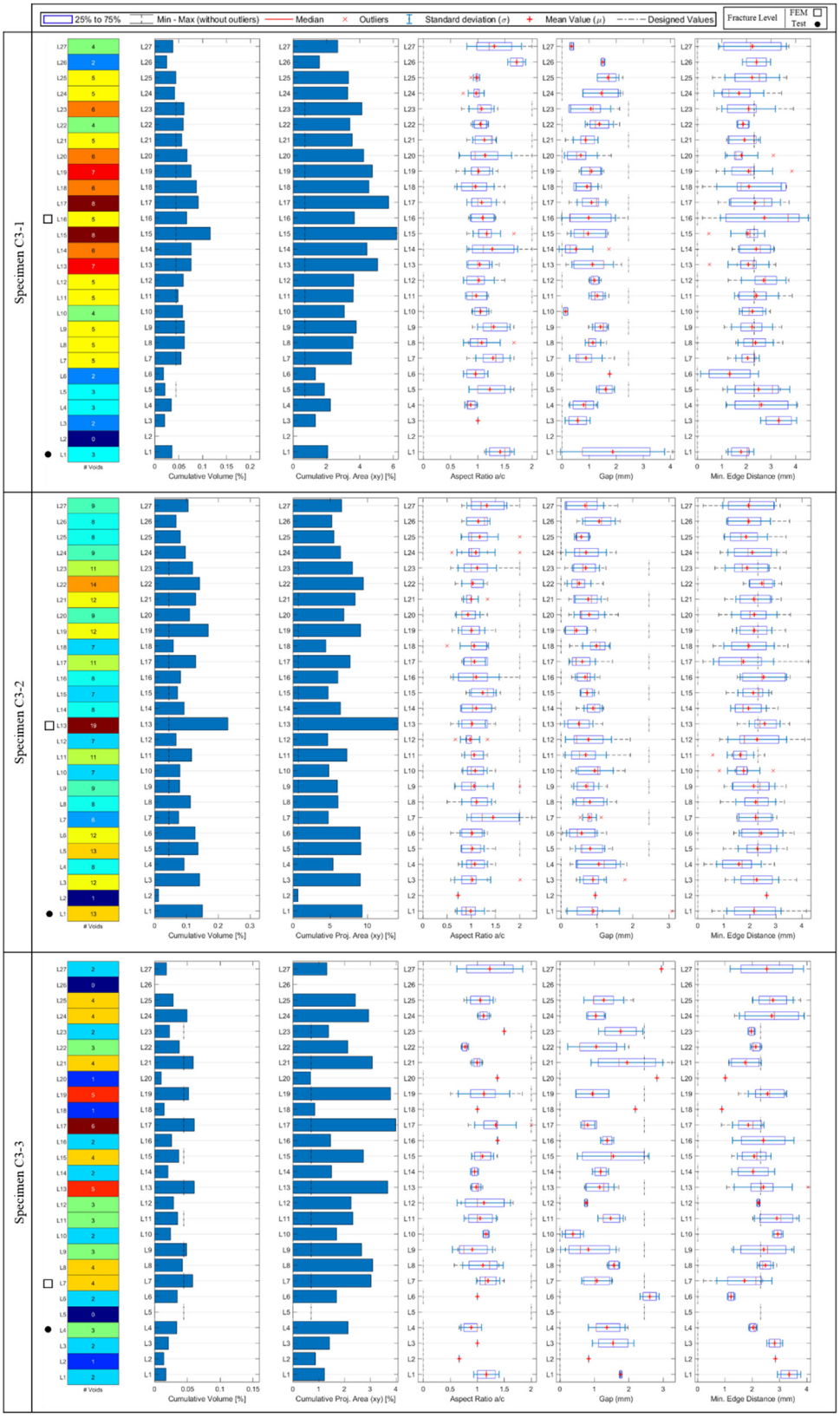

Fig. H – Summary of statistics of the XRCT porosity analysis of C3 specimens. Results of each level are displayed highlighting the fracture level and FEM prediction.

Fig. I – Fracture image of each AlSi10Mg specimen.

REFERENCES

[1] Raabe D, Tasan CC, Olivetti EA. Strategies for improving the sustainability of structural metals. Nature 2019;575:64–74. https://doi.org/10.1038/s41586-019-1702-5.

[2] Blakey-Milner B, Gradl P, Snedden G, Brooks M, Pitot J, Lopez E, et al. Metal additive manufacturing in aerospace: a review. Mater Des 2021;209:110008. https://doi.org/10.1016/j.matdes.2021.110008.

[3] Braga DFO, Tavares SMO, Da Silva LFM, Moreira PMGP, De Castro PMST. Advanced design for lightweight structures: review and prospects. Prog Aero Sci 2014;69:29–39. https://doi.org/10.1016/j.paerosci.2014.03.003.

[4] Kholgh Eshkalak S, Rezvani Ghomi E, Dai Y, Choudhury D, Ramakrishna S. The role of three-dimensional printing in healthcare and medicine. Mater Des 2020;194:108940. https://doi.org/10.1016/j.matdes.2020.108940.

[5] Salmi M. Additive manufacturing processes in medical applications. Materials 2021;14:1–16. https://doi.org/10.3390/ma14010191.

[6] Buj-Corral I, Tejo-Otero A, Fenollosa-Artés F. Development of AM technologies for metals in the sector of medical implants. Metals 2020;10:686. https://doi.org/10.3390/met10050686.

[7] Taub A, De Moor E, Luo A, Matlock DK, Speer JG, Vaidya U. Materials for automotive lightweighting. Annu Rev Mater Res 2019;49:327–59. https://doi.org/10.1146/annurev-matsci-070218-010134.

[8] Briard T, Segonds F, Zamariola N, DfAM G-. A methodological proposal of generative design for additive manufacturing in the automotive industry. Int J Interact Des Manuf 2020;14:875–86. https://doi.org/10.1007/s12008-020-00669-6.

[9] du Plessis A, Broeckhoven C, Yadroitsava I, Yadroitsev I, Hands CH, Kunju R, et al. Beautiful and functional: a review of biomimetic design in additive manufacturing. Addit Manuf 2019;27:408–27. https://doi.org/10.1016/j.addma.2019.03.033.

[10] Liu J, Gaynor AT, Chen S, Kang Z, Suresh K, Takezawa A, et al. Current and future trends in topology optimization for additive manufacturing. Struct Multidiscip Optim 2018;57:2457–83. https://doi.org/10.1007/s00158-018-1994-3.

[11] Meng L, Zhang W, Quan D, Shi G, Tang L, Hou Y, et al. From topology optimization design to additive manufacturing: today's success and tomorrow's roadmap. Arch Comput Methods Eng 2020;27:805–30. https://doi.org/10.1007/s11831-019-09331-1.

[12] Zhu JH, Zhang WH, Xia L. Topology optimization in aircraft and aerospace structures design. Arch Comput Methods Eng 2016;23:595–622. https://doi.org/10.1007/s11831-015-9151-2.

[13] Plocher J, Panesar A. Review on design and structural optimisation in additive manufacturing: towards next-generation lightweight structures. Mater Des 2019;183. https://doi.org/10.1016/j.matdes.2019.108164.

[14] Li S, Xin Y, Yu Y, Wang Y. Design for additive manufacturing from a force-flow perspective. Mater Des 2021;204:109664. https://doi.org/10.1016/j.matdes.2021.109664.

[15] Guddati S, Kiran ASK, Leavy M, Ramakrishna S. Recent advancements in additive manufacturing technologies for porous material applications. Int J Adv Manuf Technol 2019;105:193–215. https://doi.org/10.1007/s00170-019-04116-z.

[16] Lu C, Zhang C, Wen P, Chen F. Mechanical behavior of Al–Si10–Mg gyroid surface with variable topological parameters fabricated via laser powder bed fusion. J Mater Res Technol 2021;15:5650–61. https://doi.org/10.1016/j.jmrt.2021.11.008.

[17] du Plessis A. Effects of process parameters on porosity in laser powder bed fusion revealed by X-ray tomography. Addit Manuf 2019;30:100871. https://doi.org/10.1016/j.addma.2019.100871.

[18] Zhang B, Li Y, Bai Q. Defect Formation mechanisms in selective laser melting: a review. Chin J Mech Eng 2017;30:515–27. https://doi.org/10.1007/s10033-017-0121-5.

[19] Gordon JV, Narra SP, Cunningham RW, Liu H, Chen H, Suter RM, et al. Defect structure process maps for laser powder bed fusion additive manufacturing. Addit Manuf 2020;36:101552. https://doi.org/10.1016/j.addma.2020.101552.

[20] Liu J, Wen P. Metal vaporization and its influence during laser powder bed fusion process. Mater Des 2022;215:110505. https://doi.org/10.1016/j.matdes.2022.110505.

[21] Weingarten C, Buchbinder D, Pirch N, Meiners W, Wissenbach K, Poprawe R. Formation and reduction of hydrogen porosity during selective laser melting of AlSi10Mg. J Mater Process Technol 2015;221:112–20. https://doi.org/10.1016/j.jmatprotec.2015.02.013.

[22] Aboulkhair NT, Everitt NM, Ashcroft I, Tuck C. Reducing porosity in AlSi10Mg parts processed by selective laser melting. Addit Manuf 2014;1:77–86. https://doi.org/10.1016/j.addma.2014.08.001.

[23] Yang T, Liu T, Liao W, MacDonald E, Wei H, Zhang C, et al. Laser powder bed fusion of AlSi10Mg: influence of energy intensities on spatter and porosity evolution, microstructure and mechanical properties. J Alloys Compd 2020;849:156300. https://doi.org/10.1016/j.jallcom.2020.156300.

[24] Yu W, Sing SL, Chua CK, Tian X. Influence of re-melting on surface roughness and porosity of AlSi10Mg parts fabricated by selective laser melting. J Alloys Compd 2019;792:574–81. https://doi.org/10.1016/j.jallcom.2019.04.017.

[25] du Plessis A, Yadroitsava I, Yadroitsev I. Effects of defects on mechanical properties in metal additive manufacturing: a review focusing on X-ray tomography insights. Mater Des 2020;187:108385. https://doi.org/10.1016/j.matdes.2019.108385.

[26] Valdez M, Kozuch C, Faierson EJ, Jasiuk I. Induced porosity in Super Alloy 718 through the laser additive manufacturing process: microstructure and mechanical properties. J Alloys Compd 2017;725:757–64. https://doi.org/10.1016/j.jallcom.2017.07.198.

[27] Al-Maharma AY, Patil SP, Markert B. Effects of porosity on the mechanical properties of additively manufactured components: a critical review. Mater Res Express 2020;7. https://doi.org/10.1088/2053-1591/abcc5d.

[28] Laursen CM, DeJong SA, Dickens SM, Exil AN, Susan DF, Carroll JD. Relationship between ductility and the porosity of additively manufactured AlSi10Mg. Mater Sci Eng 2020;795:139922. https://doi.org/10.1016/j.msea.2020.139922.

[29] Bao J, Wu S, Withers PJ, Wu Z, Li F, Fu Y, et al. Defect evolution during high temperature tension-tension fatigue of SLM AlSi10Mg alloy by synchrotron tomography. Mater Sci Eng 2020;792:139809. https://doi.org/10.1016/j.msea.2020.139809.

[30] Johnson QC, Laursen CM, Spear AD, Carroll JD, Noell J. Analysis of the interdependent relationship between porosity , deformation , and crack growth during compression loading of LPBF AlSi10Mg. Mater Sci Eng, A 2022;852:143640. https://doi.org/10.1016/j.msea.2022.143640.

[31] Choren JA, Heinrich SM, Silver-Thorn MB. Young's modulus and volume porosity relationships for additive manufacturing applications. J Mater Sci 2013;48:5103–12. https://doi.org/10.1007/s10853-013-7237-5.

[32] Wang X, Zhao L, Fuh JYH, Lee HP. Effects of statistical pore characteristics on mechanical performance of selective laser melted parts: X-ray computed tomography and

micromechanical modeling. Mater Sci Eng 2022;834:142515. https://doi.org/10.1016/j.msea.2021.142515.
[33] Zhang Y, Zheng J, Xia Y, Shou H, Tan W, Han W, et al. Porosity quantification for ductility prediction in high pressure die casting AM60 alloy using 3D X-ray tomography. Mater Sci Eng 2020;772:138781. https://doi.org/10.1016/j.msea.2019.138781.
[34] Lordan E, Lazaro-Nebreda J, Zhang Y, Dou K, Blake P, Fan Z. On the relationship between internal porosity and the tensile ductility of aluminium alloy die-castings. Mater Sci Eng 2020;778:139107. https://doi.org/10.1016/j.msea.2020.139107.
[35] Garlea E, Choo H, Sluss CC, Koehler MR, Bridges RL, Xiao X, et al. Variation of elastic mechanical properties with texture, porosity, and defect characteristics in laser powder bed fusion 316L stainless steel. Mater Sci Eng 2019;763:138032. https://doi.org/10.1016/j.msea.2019.138032.
[36] Liu W, Chen C, Shuai S, Zhao R, Liu L, Wang X, et al. Study of pore defect and mechanical properties in selective laser melted Ti6Al4V alloy based on X-ray computed tomography. Mater Sci Eng 2020;797:139981. https://doi.org/10.1016/j.msea.2020.139981.
[37] Charalampous P, Kostavelis I, Tzovaras D. Non-destructive quality control methods in additive manufacturing: a survey. Rapid Prototyp J 2020;26:777–90. https://doi.org/10.1108/RPJ-08-2019-0224.
[38] Du Plessis A, Yadroitsev I, Yadroitsava I, Le Roux SG. X-ray microcomputed tomography in additive manufacturing: a review of the current technology and applications. 3D Print Addit Manuf 2018;5:227–47. https://doi.org/10.1089/3dp.2018.0060.
[39] Wang P, Lei H, Zhu X, Chen H, Fang D. Influence of manufacturing geometric defects on the mechanical properties of AlSi10Mg alloy fabricated by selective laser melting. J Alloys Compd 2019;789:852–9. https://doi.org/10.1016/j.jallcom.2019.03.135.
[40] Doroszko M, Falkowska A, Seweryn A. Image-based numerical modeling of the tensile deformation behavior and mechanical properties of additive manufactured Ti–6Al–4V diamond lattice structures. Mater Sci Eng 2021;818:141362. https://doi.org/10.1016/j.msea.2021.141362.
[41] Zhou M, Zhou H. Experimental investigation and numerical modeling of strength properties of iron ore sinter based on pilot-scale pot tests and X-ray computed tomography. J Mater Res Technol 2020;9:13106–17. https://doi.org/10.1016/j.jmrt.2020.09.054.
[42] Khrapov D, Koptyug A, Manabaev K, Léonard F, Mishurova T, Bruno G, et al. The impact of post manufacturing treatment of functionally graded Ti6Al4V scaffolds on their surface morphology and mechanical strength. J Mater Res Technol 2020;9:1866–81. https://doi.org/10.1016/j.jmrt.2019.12.019.
[43] Trevisan F, Calignano F, Lorusso M, Pakkanen J, Aversa A, Ambrosio EP, et al. On the selective laser melting (SLM) of the AlSi10Mg alloy: process, microstructure, and mechanical properties. Materials 2017;10. https://doi.org/10.3390/ma10010076.
[44] Yap CY, Chua CK, Dong ZL, Liu ZH, Zhang DQ, Loh LE, et al. Review of selective laser melting: materials and applications. Appl Phys Rev 2015;2:041101. https://doi.org/10.1063/1.4935926.
[45] Liverani E, Zanini F, Tonelli L, Carmignato S, Fortunato A. The influence of geometric defects and microstructure in the simulation of the mechanical behaviour of laser powder-bed fusion components: application to endoprosthesis. J Manuf Process 2021;71:541–9. https://doi.org/10.1016/j.jmapro.2021.09.043.
[46] Raghavendra S, Molinari A, Dallago M, Zappini G, Zanini F, Carmignato S, et al. Uniaxial static mechanical properties of regular, irregular and random additively manufactured cellular materials: nominal vs. real geometry. Forces Mech 2021;2:100007. https://doi.org/10.1016/j.finmec.2020.100007.
[47] du Plessis A, Yadroitsava I, le Roux SG, Yadroitsev I, Fieres J, Reinhart C, et al. Prediction of mechanical performance of Ti6Al4V cast alloy based on microCT-based load simulation. J Alloys Compd 2017;724:267–74. https://doi.org/10.1016/j.jallcom.2017.06.320.
[48] Wang P, Zhou H, Zhang L, Chen H, Zhu X, Lei H, et al. In situ X-ray micro-computed tomography study of the damage evolution of prefabricated through-holes in SLM-Printed AlSi10Mg alloy under tension. J Alloys Compd 2020;821:153576. https://doi.org/10.1016/j.jallcom.2019.153576.
[49] Galbusera F, Cina A, Panico M, Albano D, Messina C. Image-based biomechanical models of the musculoskeletal system. Eur Radiol Exp 2020;4. https://doi.org/10.1186/s41747-020-00172-3.
[50] Young PG, Beresford-West TBH, Coward SRL, Notarberardino B, Walker B, Abdul-Aziz A. An efficient approach to converting three-dimensional image data into highly accurate computational models. Phil Trans Math Phys Eng Sci 2008;366:3155–73. https://doi.org/10.1098/rsta.2008.0090.
[51] Hitzler L, Janousch C, Schanz J, Merkel M, Heine B, Mack F, et al. Direction and location dependency of selective laser melted AlSi10Mg specimens. J Mater Process Technol 2017;243:48–61. https://doi.org/10.1016/j.jmatprotec.2016.11.029.
[52] SLM Solutions. Material data sheet Al-alloy AISi10Mg, vol. 7. SLM Solutions Group AG; 2019.
[53] Hooputra H, Gese H, Dell H, Werner H. A comprehensive failure model for crashworthiness simulation of aluminium extrusions. Int J Crashworthiness 2004;9:449–64.
[54] Bai Y, Wierzbicki T. A new model of metal plasticity and fracture with pressure and Lode dependence. Int J Plast 2008;24:1071–96. https://doi.org/10.1016/j.ijplas.2007.09.004.
[55] Palumbo B, Del Re F, Martorelli M, Lanzotti A, Corrado P. Tensile properties characterization of AlSi10Mg parts produced by direct metal laser sintering via nested effects modeling. Materials 2017;10. https://doi.org/10.3390/ma10020144.
[56] Costas M, Morin D, de Lucio M, Langseth M. Testing and simulation of additively manufactured AlSi10Mg components under quasi-static loading. Eur J Mech A/Solids 2020;81. https://doi.org/10.1016/j.euromechsol.2020.103966.
[57] Delahaye J, Tchuindjang JT, Lecomte-Beckers J, Rigo O, Habraken AM, Mertens A. Influence of Si precipitates on fracture mechanisms of AlSi10Mg parts processed by Selective Laser Melting. Acta Mater 2019;175:160–70. https://doi.org/10.1016/j.actamat.2019.06.013.
[58] Kempf A, Hilgenberg K. Influence of sub-cell structure on the mechanical properties of AlSi10Mg manufactured by laser powder bed fusion. Mater Sci Eng A 2020;776:138976. https://doi.org/10.1016/j.msea.2020.138976.